A hybrid numerical/analytic technique for the computation of wave fields in stratified media based on the Hankel transform

Douglas R. Mook[a)]
Research Laboratory of Electronics, Massachusetts Institute of Technology, Cambridge, Massachusetts 02139 and Woods Hole Oceanographic Institution, Woods Hole, Massachusetts 02543

George V. Frisk
Woods Hole Oceanographic Institution, Woods Hole, Massachusetts 02543

Alan V. Oppenheim
Research Laboratory of Electronics, Massachusetts Institute of Technology, Cambridge, Massachusetts 02139

(Received 3 August 1983; accepted for publication 7 March 1984)

A hybrid numerical/analytic technique is presented for computing the field due to a monochromatic point source in a horizontally stratified medium. It is based on the exact Hankel transform relationship between the field in the range domain and the associated depth-dependent Green's function in the horizontal wavenumber domain. The method uses a numerical evaluation of the Hankel transform. It is shown that a major source of error in such an evaluation arises from undersampling of the Green's function at points where it becomes infinite. This error is described in terms of aliasing, analogous to the aliasing that has been well-described for the discrete Fourier transform. It is shown that the error can be substantially reduced by removing the infinities, calculating the Hankel transform of the remaining portion of the Green's function numerically, and adding to it the analytically computed Hankel transform of the infinities. The sum of the analytic terms and the remaining Hankel transform always exactly equals the true field with no errors introduced other than those associated with the numerical evaluation of the Hankel transform, and the method is accurate in both the near- and farfield regions. The technique is developed in detail for the acoustics problem of a monochromatic point source and receiver in an isovelocity fluid half-space overlying a horizontally stratified fluid medium. It is found that under circumstances of interest in ocean bottom acoustics, where the Green's function has only a few singularities along the real horizontal wavenumber axis, the technique is efficient and extremely accurate.

PACS numbers: 43.30.Bp, 43.30.Dr, 43.20.Bi, 43.20.Fn

INTRODUCTION

The calculation of wave fields due to a monochromatic point source in a horizontally stratified medium is a problem of fundamental importance in acoustics, seismics, and electromagnetics.[1–5] It is essential for the prediction of fields under a variety of circumstances and for the proper interpretation of experimental measurements. It is also useful in the study of the inverse problem in which field measurements are used to infer properties of the medium. Presently, techniques for the generation of synthetic fields fall into three broad categories—modal, ray, and numerical. In modal and ray techniques, numerical methods typically play a secondary role in the sense that they are used to compute contributions to the field which are not readily accommodated within the modal or ray analytic framework or to perform portions of the calculations which cannot be executed analytically. Numerical techniques are founded upon direct numerical evaluation of integrals and are often used in complicated situations where analytic methods are intractable. Numerical methods are sometimes used to check analytic methods, a procedure which may fail to recognize that sources of numerical error can be at least as large and subtle as sources of error arising from analytic approximations.

This paper presents a hybrid numerical/analytic technique for computing the field due to a monochromatic point source in a horizontally stratified medium. It is based upon the numerical evaluation of the Hankel transform that relates the depth-dependent Green's function in the horizontal wavenumber domain to the field in the range domain. We show that a major source of error in such an evaluation arises from undersampling at the points where the depth-dependent Green's function becomes infinite. We describe this error in terms of aliasing, analogous to the degradation due to sampling that has been well described for the Fourier transform.[6] We show that these errors can be substantially reduced by removing the infinities, numerically computing the Hankel transform of the remaining portion of the Green's function and adding to it the analytically determined Hankel transform of the infinities. Such a procedure does not require the artificial introduction of absorption into the medium in order to diffuse the infinities. The numerical contribution is subordinate to the analytically determined terms for large ranges, minimizing the effects of aliasing. The sum of the analytic parts and the remaining Hankel transform always exactly equals the true field and no approximations are made until the Hankel transform is performed numerically. Unlike standard modal methods the contribution associated

[a)] Present address: Sanders Associates, Inc., MER24-1583C, Nashua, NH 03061-2034.

 0001-4966/84/070222-22$00.80

with each mode is finite, even at zero range (except, of course, at the source point itself) and explicit branch line integrals do not appear. The technique includes the evanescent portion of the Green's function and accurately generates the effects due to trapped modes which can dominate the field for large offsets because of their slow asymptotic decay. It is thus accurate in both the near- and farfield regions.

The method presented was developed in the context of the canonical acoustics problem of a monochromatic point source and receiver in an isovelocity fluid half-space overlying a horizontally stratified fluid medium, and we will concentrate upon this case. It is of great interest in the study of forward and inverse problems in ocean bottom acoustics and seismics,[7–10] and specific examples considered in this paper are closely tied to parameters encountered in experimental data.[11] For this class of problems, where the Green's function has only a few infinities to be removed, the method has been found to be efficient and extremely accurate. It can also be applied to other situations, such as more complicated cases that include shear wave effects (and the poles that they introduce). The procedure becomes more lengthy as the number of infinities increases, however, since their precise horizontal wavenumbers are required in the calculation.

A great deal of this work revolves around the Hankel transform and its numerical implementation. Presently there exist a variety of numerical implementations in the literature[7,12–24] but no one standard comparable to the fast Fourier transform as an implementation of the Fourier transform. In this paper we will use three different implementations. The Fourier–Bessel series[24] is used for many of the computations because its properties have been well studied[24–26] and because we have been able to characterize its aliasing properties. Its principal limitation is that it is quite slow. We also consider a common asymptotic algorithm[27,12,13] in order to derive and illustrate an aliasing result. This asymptotic algorithm casts the Hankel transform into the form of a Fourier transform and consequently is useful for translating many of the results available for the Fourier transform into approximate results for the Hankel transform. It is also often used in practice.[12,13] Finally we use a third algorithm to generate the field for a realistic ocean bottom example with a large source height.[21,7] This algorithm is extremely fast which makes it possible to sample the Green's function with sufficient density to minimize the effect of aliasing on the numerically performed transform. In addition to its speed this algorithm is appropriate for the generation of synthetic data because it uses samples on a square root grid which, as will be shown, is an excellent grid for the representation of the Green's function.

In this paper we have focused on the time-independent, harmonic problem rather than the more general time-dependent problem. The general time-dependent problem can be solved by generating harmonic fields over a band of frequencies corresponding to the source spectrum which are then combined to generate the time-dependent field. We have concentrated on the time-independent problem in order to focus on the issues associated with this crucial first step.

Section I is a background section which includes a brief discussion of the relationship of our method to modal and ray techniques. Section II concentrates on the numerical evaluation of the Hankel transform. Aliasing results are derived and the resultant serious degradation of synthetic fields generated by direct numerical methods is demonstrated. Section III presents a hybrid method for the generation of synthetic fields that decay as $1/r$, where r is the horizontal range between source and receiver. This method is demonstrated for a hard bottom and slow and fast isovelocity bottom examples. It is then generalized to the generation of synthetic fields that decay as $1/\sqrt{r}$, which arise when slow isovelocity layers are present. Section IV discusses the fast Hankel transform algorithm and applies it to the generation of synthetic data for a realistic ocean bottom acoustic sound speed profile and experimental geometry. The result is compared to that produced by a conventional ray technique.

I. BACKGROUND

We consider a horizontally stratified medium characterized by one-dimensional variations of density and sound speed in the cylindrical coordinate z. For such a medium, the spatial part of the acoustic pressure variation P, due to a point source with time dependence $e^{-i\omega t}$, is related to the depth-dependent Green's function G, through the zero-order Hankel transform[13,8]:

$$P(r) = \int_0^\infty G(k_r)\, J_0(k_r r) k_r\, dk_r, \tag{1}$$

$$G(k_r) = \int_0^\infty P(r)\, J_0(k_r r) r\, dr, \tag{2}$$

where r is the horizontal range, k_r is the horizontal wavenumber, and $J_0(\cdot)$ is the Bessel function of order zero. In the case depicted in Fig. 1, of interest in ocean acoustics, both source and receiver are located in a region of thickness h, characterized by a constant density, a sound speed $c(z)$, and wavenumber $k(z) = \omega/c(z)$. The layer may be bounded at both top and bottom by horizontally stratified media. Under these circumstances, P satisfies[8]

$$\left[\frac{1}{r}\frac{\partial}{\partial r}\left(r\frac{\partial}{\partial r}\right) + \frac{\partial^2}{\partial z^2} + k^2(z)\right] P(r; z, z_0) = -2[\delta(r)/r]\delta(z - z_0), \tag{3}$$

while G satisfies

$$\left(\frac{d^2}{dz^2} + k^2(z) - k_r^2\right) G(k_r; z, z_0) = -2\delta(z - z_0), \tag{4}$$

along with impedance boundary conditions at the top and the bottom. Although both P and G depend on the source and receiver heights above the bottom, z and z_0, these heights will be viewed as parameters in the problem, while r and k_r will act as the conjugate transform variables.

The different techniques for computing fields in stratified media can be divided into the classes of modal methods, ray methods, and numerical methods. These can be viewed as arising from different approaches to the evaluation of the integral in Eq. (1). In this section we present a brief overview of these methods. Our presentation is brief because detailed descriptions of modal, ray, and numerical methods can be

found elsewhere.[1–5,28,13,7]

In order to illustrate the major features of interest we will discuss two simplifications of the profile shown in Fig. 1. In the first more general case we will consider the water to be isovelocity so that the water column with boundaries acts as a (possibly leaky) waveguide. The method that we will develop can be used to accommodate this model. Most of our presentation in this paper, however, will concentrate on a simplified version of this model, where the top has been removed. Such a simplified model is often appropriate in deep ocean acoustics where the return from the surface can be gated out in time.[11]

For the more general case for which a surface boundary has been specified, $G(k_r)$ in Eq. (4) is given by[1]

$$G(k_r) = (i\{\exp(i\sqrt{k_0^2 - k_r^2}\,|z - z_0|) + \Gamma_B \exp(i\sqrt{k_0^2 - k_r^2}\,|z + z_0|) + \Gamma_T \exp(2i\sqrt{k_0^2 - k_r^2}\,h)$$
$$\times \left[\exp(-i\sqrt{k_0^2 - k_r^2}\,|z + z_0|) + \Gamma_B \exp(-i\sqrt{k_0^2 - k_r^2}\,|z - z_0|)\right]\})$$
$$\times \{\sqrt{k_0^2 - k_r^2}\left[1 - \Gamma_T \Gamma_B \exp(2i\sqrt{k_0^2 - k_r^2}\,h)\right]\}^{-1}, \tag{5}$$

where k_0 is the wavenumber in the layer and Γ_T and Γ_B are the plane-wave reflection coefficients at the top and bottom, respectively.

In the more restricted case where $\Gamma_T(k_r) = 0$, it is common to separate out the contribution, $G_I(k_r)$, of the incident field to the Green's function

$$G_I(k_r) = (i/\sqrt{k_0^2 - k_r^2})\exp(i\sqrt{k_0^2 - k_r^2}\,|z - z_0|), \tag{6}$$

since that term can be integrated analytically, and to consider only that portion of the Green's function associated with the reflected return. This is given by

$$G(k_r) = (i/\sqrt{k_0^2 - k_r^2})\Gamma_B(k_r)\exp(i\sqrt{k_0^2 - k_r^2}\,|z + z_0|). \tag{7}$$

In modal methods, the path of integration along the real k_r axis is viewed as a portion of a closed contour in the complex k_r plane. The calculation then amounts to determining the residues at the poles enclosed by the contour and the contributions of branch cuts along the contour.[29–33] The method is intimately connected with the analytic properties of G, specifically its pole and branch point singularities. For example, the poles occur at the zeros of $1 - \Gamma_T \Gamma_B \exp(2i\sqrt{k_0^2 - k_r^2}\,h)$ for the more general case with a top and $1/\Gamma_B$ for the restricted case without a top. These poles correspond physically to the free modes of vibration of the system and have a characteristic $1/\sqrt{r}$ falloff. Branch points occur at the wavenumbers associated with any isovelocity half-space. In some cases their contribution can be interpreted physically as lateral waves, which have a $1/r^2$ decay. Since the residue contributions have a closed form expression, no numerical integration is required. The branch line contributions must be evaluated numerically in general and these calculations can be computationally expensive and/or corrupted by numerical sources of error. Fortunately for many applications branch line contributions can be ignored in the farfield. In the nearfield where branch line integrals must be included, modal methods also suffer from the fact that the residue contribution of each pole has a logarithmic singularity at the origin. Since outside the plane of the source ($z \neq z_0$) the field is not infinite in general, any singularity introduced by a residue contribution must be canceled by a singular value from the numerically performed branch line integral or from the contribution of other poles. It is not possible to generate an infinite value as the output of a numerical algorithm, and adding and subtracting large contributions is subject to severe numerical errors. Consequently for small ranges the total field calculated may be seriously degraded even when the contribution from the branch line is included. For large ranges no numerical integration is required and this problem does not arise. Consequently modal methods are frequently used for farfield calculations, particularly in waveguides (Γ_T and Γ_B both nonzero) where the modes quickly dominate the total field. Modal methods are often not appropriate when the field must be calculated for small ranges or when one or both of the reflection coefficients, $\Gamma_T(k_r)$ and $\Gamma_B(k_r)$ are sufficiently

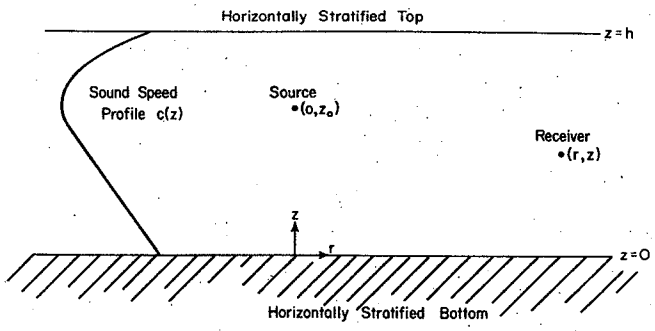

FIG. 1. Horizontally stratified ocean model.

small that the continuous spectrum (branch line contribution) dominates the field. Also when the number of propagating modes becomes too large to conveniently determine their position and residues, then modal methods become cumbersome and questions arise concerning the number of modes that must be included for accurate field calculations.[34] When the problem is simply that there are too many contributing modes but none dominate, then other conventional methods are available.

In ray methods[35] the denominator of G (for the case with the top) is expanded as[36]

$$\left[1-\Gamma_T\Gamma_B \exp(2i\sqrt{k_0^2-k_r^2}\,h)\right]^{-1}$$

$$=\sum_{n=0}^{\infty}\left[\Gamma_T\Gamma_B \exp(2i\sqrt{k_0^2-k_r^2}\,h)\right]^n. \tag{8}$$

This procedure eliminates the poles of interest in the modal approach, but results in a series of integrals which may have branch points. Each integral is evaluated by deforming the path of integration in the complex plane to follow lines of steepest descent, thereby concentrating the contributing portions of the integral to short arcs.[1] If approximate results are satisfactory then the integrand is approximated by a Taylor expansion on these arcs and the resulting expansion is integrated analytically. If more accuracy is required the integrals must be performed numerically.[2] The contribution from each arc can be interpreted as a ray, while the branch line integrals picked up in the process of contour deformation again correspond to lateral waves. Each ray represents the constructive interference of many modes,[37] both proper and improper. Because the approximate expressions for the rays can be computed analytically such an expansion is efficient when these are sufficient. Ray techniques are often reasonable for those cases where many propagating modes exist but none dominate. Such is the case when the material parameters vary slowly compared to a wavelength. When great accuracy is required and the integration along the steepest descent paths are performed numerically, ray techniques can become very expensive to evaluate. In the limit of long numerical integrals they do not offer a substantial advantage over direct numerical methods and suffer from the loss of the form of the Hankel transform.

For cases where no modes propagate and the continuous spectrum dominates, direct numerical methods are used to evaluate the Hankel transform along the real axis. On occasion the integral is evaluated by direct numerical quadrature.[38,39] Frequently it is evaluated approximately by replacing the Bessel function with its asymptotic form.[27,12,13] This converts the original integral into a related integral that can be evaluated efficiently with a fast Fourier transform. Typically the evanescent portion of the spectrum is ignored in these methods. At present, direct numerical methods fail when trapped modes caused by slow speed layers or other waveguide effects become important even when the evanescent spectrum is included in the integration.[7]

Modal methods are most suitable when a manageable number of trapped modes represent the field and only the farfield is desired. Ray methods are suitable for cases where the interference patterns of many modes can be well represented by rays and no few modes alone dominate the field. When the combined effect of evanescent modes is important (as is the case for small range calculations or propagation along a low impedance contrast boundary) and there are some important guided modes (such as may arise from a low speed layer in the bottom of the ocean or in the atmosphere for electromagnetic propagation) there is currently no generally available accurate, efficient means of generating fields.

Our approach stems from a need to generate fields accurately for both near- and farfields where there may exist some important guided modes. We chose to concentrate on a direct numerical evaluation of the Hankel transform to accurately include the effects of the continuous spectrum. Within this context we are therefore interested in the analytic properties of the Green's function to the extent that they may degrade the numerical integration scheme. From this point of view, we concentrate on the singularities of $G(k_r)$ insofar as they affect the sampling required to adequately determine their contribution to the integral. It is not sufficient to simply increase the sampling rate until the result converges. At best that approach is extremely time consuming; often it is a practical impossibility. Also we avoided the artificial introduction of absorption into the problem which would have pushed the singularities off the axis of integration. We felt that in order to adequately solve the aliasing problem in this manner it was necessary to introduce so much attenuation that the original problem was significantly changed, or if the deformation of the contour was compensated for by multiplying the resulting field by a growing exponential, then any numerical noise, including aliasing, would be enhanced and in general little would be gained. We chose, instead, to remove the singularities and to compute their effect analytically, thereby leaving a numerical integration that was well-behaved.

The singularities removed are due to the $i/\sqrt{k_0^2-k_r^2}$ source term and the poles in the Green's function on the real k_r axis. Removing the $i/\sqrt{k_0^2-k_r^2}$ term and calculating its contribution generates a term that decays as $1/r$. The poles contribute modal-type fields which decay as $1/\sqrt{r}$, but are finite even for zero range, unlike conventional modal fields. In this decomposition of the field, explicit branch line integrals do not appear. Their contribution is distributed between the numerical and analytic calculations in a manner such that both are finite for zero range.

One additional consideration in the numerical evaluation of the Hankel transform is the point at which the integral is truncated. The Green's function for the case of interest in Eq. (7) is effectively truncated when $|z+z_0|>0$ for $k_r>k_0$ because of the exponential source–receiver term which becomes $\exp(-\sqrt{k_r^2-k_0^2}\,|z+z_0|)$ in this region except possibly for the contribution of poles where the reflection coefficient becomes infinite. As long as the integration window in k_r includes at least some of this region of rapid exponential decay and any poles (which occur for $k_r>k_0$) are properly accounted for, the errors due to a finite aperture are minimal. The special case $|z+z_0|=0$ is not discussed here.

II. ALIASING AND THE NUMERICAL EVALUATION OF THE HANKEL TRANSFORM

In this section we consider the effect of numerically integrating the Hankel transform.[40,41,24] In particular we consider the degradation introduced by replacing the integral with a sum. We restrict our attention to integration techniques that are exact when the function to be transformed is bandlimited and the sampling rate is sufficiently high.[42]

In this section we derive the error associated with the numerical evaluation of the Hankel transform through its asymptotic form. In Appendix A we derive an analogous result for the case where the Fourier–Bessel series is used to evaluate the Hankel transform. The results are qualitatively similar and characterize the error associated with bandlimited integration of the Hankel transform on an even or approximately even grid. By analogy to the Fourier transform we will refer to the errors introduced by violation of the bandlimited assumption as aliasing.

When the Hankel transform is evaluated approximately as a Fourier transform using the asymptotic form for the Bessel function and a FFT, the resulting aliasing can be determined from well known results for the Fourier transform. Upon replacement of the Bessel function with its asymptotic form in the Hankel transform, Eq. (1) becomes

$$P_a(r) = (\sqrt{2}/\sqrt{\pi r}) \int_0^\infty G(k_r)\cos(k_r r - \pi/4)\sqrt{k_r}\, dk_r, \quad (9)$$

or, expanding the cosine term,

$$\sqrt{r}P_a(r) = f_c(r) + f_s(r), \quad (10)$$

where $f_c(r)$ and $f_s(r)$ are the Fourier cosine and sine transforms of $\sqrt{k_r}\,G(k_r)$, respectively,

$$f_c(r) = (1/\sqrt{\pi}) \int_0^\infty [G(k_r)\sqrt{k_r}\,]\cos(k_r r)dk_r,$$
$$f_s(r) = (1/\sqrt{\pi}) \int_0^\infty [G(k_r)\sqrt{k_r}\,]\sin(k_r r)dk_r. \quad (11)$$

Note that $P_a(r)$ is not even, unlike $P(r)$. This approximation can be valid only for $r > 0$.

When these Fourier integrals are evaluated using a discrete Fourier transform with a sampling period T, the result is an aliased signal[6]:

$$[\sqrt{r}\,\hat{P}_a(r)] = \sum_n f_c\left(r - \frac{n}{T}\right) + \sum_n f_s\left(r - \frac{n}{T}\right)$$
$$= \sum_n \sqrt{r - \frac{n}{T}}\, P_a\left(r - \frac{n}{T}\right), \quad (12)$$

so that finally

$$\hat{P}_a(r) = \left(\frac{1}{\sqrt{r}}\right) \sum_n \sqrt{r - \frac{n}{T}}\, P_a\left(r - \frac{n}{T}\right). \quad (13)$$

The effect of aliasing on the Hankel transform (when this approximate method for evaluation is used) is to generate $1/\sqrt{r}$ times an aliased image of $\sqrt{r}P_a(r)$.

To illustrate this kind of aliasing, in Fig. 2 we show the effect of aliasing using the asymptotic method to evaluate the Hankel transform of $J_1(k_r)/k_r$ (Ref. 43). For this case the correct transform is given by

$$P(r) = \mathrm{HT}\left(\frac{J_1(k_r)}{k_r}\right) = \begin{cases} 1, & 0 < k_r < 1, \\ 0, & 1 < k_r. \end{cases} \quad (14)$$

Figure 2(a) shows the magnitude of $\sqrt{r}\hat{P}(r)$ where a sampling period of $T = 2/5$ has been assumed. This sampling period is sufficiently short that the replications of $\sqrt{r}\hat{P}(r)$ are well separated. Figure 2(b) shows the corresponding transform, $\hat{P}(r)$. As can be seen the transform is correct in the region $0 < r < 1$. Figure 2(c) and (d) present the analogous pictures for a sampling period of $T = 2/3$. This is not sufficient to prevent aliasing in the region $0 < r < 1$. Figure 2(c) shows $\sqrt{r}\hat{P}(r)$ for this case, displaying the kind of aliasing seen with the Fourier transform. Figure 2(d) shows $\hat{P}(r)$. The transform suffers from aliasing in the region $r > 1/2$.

It might be noted that even if $P(r)$ is real, $P_a(r)$ and $\hat{P}_a(r)$ will not in general be real. Further, the aliasing introduced by sampling causes the continuation of $P_a(r)$ to $r < 0$ implied by Eq. (10) to be felt in $\hat{P}_a(r)$ for $r > 0$.

If the alternate asymptotic transform for $P(r)$

$$P_a^{(2)}(r) \equiv \frac{\sqrt{2}}{\pi|r|} \int_0^\infty G(k_r)\cos\left(|k_r|r - \frac{\pi}{4}\right)\sqrt{|k_r|}\, dk_r \quad (15)$$

is used, similar but slightly more complicated results are obtained. In Appendix A the aliasing result based upon approximation of the Hankel transform by the Fourier–Bessel series also shows degradation well described in terms of a $1/\sqrt{r}$ weighting of a replicated version of $\sqrt{r}P(r)$ similar to Eq. (13), although there are sign changes. This result seems to describe the character of aliasing for numerical evaluation of the Hankel transform where linear (or approximately linear) sampling is used together with something equivalent to a bandlimited assumption.

The importance of this result for the generation of synthetic fields can be seen from the two canonical examples which follow. In these examples the numerical Hankel transforms are performed using the Fourier–Bessel series because among the exact Hankel transform algorithms the associated errors are best understood. Using the Fourier–Bessel series as an approximation to the Hankel transform, the function, $\hat{P}(r)$ is given by[24]

$$\hat{P}(r) = \frac{2}{A^2} \sum_1^N \left[G\left(\frac{\lambda_n}{A}, z, z_0\right) J_0\left(r\frac{\lambda_n}{A}\right) \Big/ J_1^2(\lambda_n) \right], \quad 0 < r < A, \quad (16)$$

where λ_n are the zeros of $J_0(\cdot)$ and $\lambda_n \approx n\pi - \pi/4$. A is the "bandwidth" of $P(r)$ in the sense that the Fourier–Bessel series exactly generates $P(r)$ as long as $P(r) = 0$ for $r > A$.

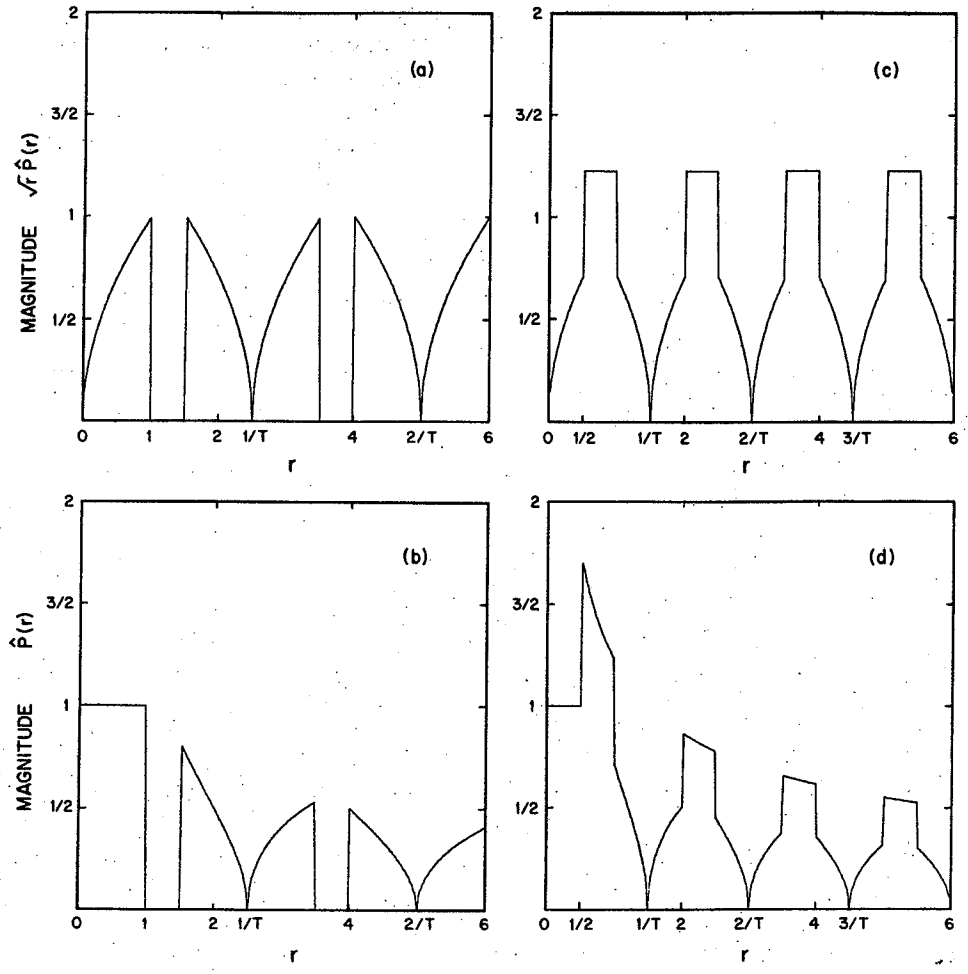

FIG. 2. Magnitude of (a) $\sqrt{r}\hat{P}(r)$ and (b) $\hat{P}(r)$ for a sampling period $T=2/5$, and magnitude of (c) $\sqrt{r}\hat{P}(r)$ and (d) $\hat{P}(r)$ for $T=2/3$.

A. Example 1

We consider the numerical evaluation of the known integral[28]:

$$P(r)=\int_0^\infty (i/\sqrt{k_0^2-k_r^2})\times\exp(i\sqrt{k_0^2-k_r^2}\,|z+z_0|)J_0(k_r r)k_r\,dk_r$$
$$=\exp[ik_0\sqrt{r^2+(z+z_0)^2}\,]/\sqrt{r^2+(z+z_0)^2}. \quad (17)$$

This integral corresponds to the reflected field generated by a point source in an isovelocity half-space over a hard bottom. Asymptotically it decays as $1/r$.

Figure 3 shows the magnitude of the result of performing the transform of Eq. (17) numerically using the Fourier–Bessel series together with the correct result. For this example the A in Eq. (16) was chosen to be $A=2000$, values of k_r were included up to $k_r \leqslant 2$, well above the start of exponential decay of the input function at $k_0=0.8976$, and $z+z_0$ was chosen to be $z+z_0=2$. The output of the Fourier–Bessel series has been displayed to twice its region of validity to better illustrate the source of degradation. We see that the magnitude of the numerically generated function $\hat{P}(r)$ oscillates rapidly, in contrast with the true Hankel transform. As we will now show these oscillations are due to aliasing in the numerically computed Hankel transform.

We showed earlier that the effect of sampling on the Hankel transform is to approximately produce an aliased estimate of the true transform $\sqrt{r}P(r)$. Since for this example, $P(r)$ decays asymptotically as $1/r$, $\sqrt{r}P(r)$ decays asymptotically only as $1/\sqrt{r}$. What we see in Fig. 3 is given approxi-

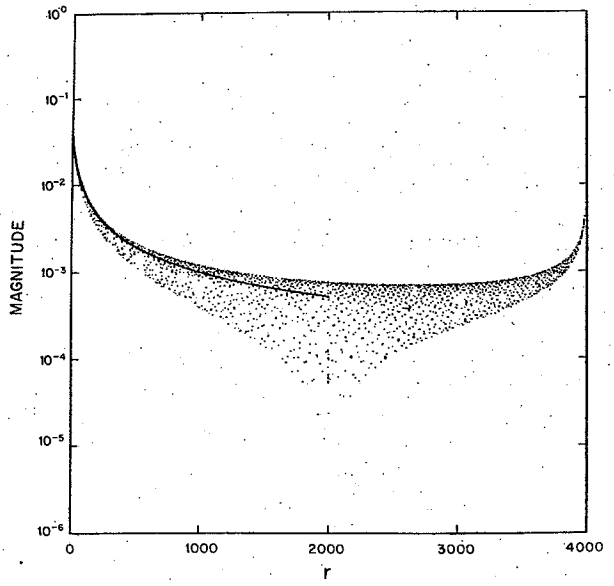

FIG. 3. Magnitude of field computed numerically using the Fourier–Bessel series (dots) compared with the exact result (solid curve) for the hard bottom example.

mately by[44]

$$0<r<2A,$$

$$|\hat{P}(r)|\approx\left|\frac{1}{\sqrt{r}}\left(\sqrt{r}\,\frac{\exp[ik_0\sqrt{r^2+(z+z_0)^2}]}{[r^2+(z+z_0)^2]^{1/2}}-\sqrt{2A-r}\,\frac{\exp[ik_0\sqrt{(2A-r)^2+(z+z_0)^2}]}{[(2A-r)^2+(z+z_0)^2]^{1/2}}\right)\right|. \tag{18}$$

When r is much greater than $z+z_0$, $\hat{P}(r)$ is approximately

$$0<r<2A,$$

$$|\hat{P}(r)|\approx|(1/\sqrt{r})(e^{ik_0r}/\sqrt{r}-e^{ik_0|2A-r|}/\sqrt{2A-r})|. \tag{19}$$

Since we are in the region $r<2A$ this can be rewritten

$$0<r<2A,$$

$$|\hat{P}(r)|\approx|(1/\sqrt{r})[e^{ik_0r}/\sqrt{r}-(e^{ik_02A}/\sqrt{2A-r})e^{-ik_0r}]|. \tag{20}$$

We can write Eq. (20) in terms of the desired transform and a modulation term as

$$|\hat{P}(r)|\approx|(1/\sqrt{r})[(1/\sqrt{r}-e^{ik_02A}/\sqrt{2A-r})e^{ik_0r}+2i(e^{ik_02A}/\sqrt{2A-r})\sin k_0r]|, \tag{21}$$

which upon defining $\epsilon(r)\equiv e^{ik_02A}/\sqrt{2A-r}$ leaves

$$|\hat{P}(\hat{r})|\approx|[1/r-\epsilon(r)/\sqrt{r}]e^{ik_0r}+2i[\epsilon(r)/\sqrt{r}]\sin k_0r|. \tag{22}$$

When $r\ll 2A$, $\epsilon(r)$ is small, so that the magnitude of $\hat{P}(r)$ appears as roughly the correct transform with a modulation term.

Frequently in practice the asymptotic form of the Hankel transform is used with a fast Fourier transform to generated synthetic fields. Since in the absence of trapped modes, the evanescent portion of the spectrum, $k_r>k_0$, is often negligible, it is reasonable and common to include just the real portion of the spectrum, $0<k_r<k_0$. When this procedure is followed the Green's function is sampled with the interval $T=k_0/N$. The field is then provided by the fast Fourier transform on the ranges

$$r=\frac{2\pi n}{2NT}=\frac{\pi n}{k_0}=n\frac{\lambda_0}{2},\quad n=0,1,2,\ldots,\frac{N}{2}, \tag{23}$$

where λ_0 is used here as the wavelength associated with the horizontal wavenumber of the layer containing the source and receiver. On this grid the $\sin(k_0r)$ term would not appear. The error would appear as a slowly varying offset in the magnitude of the pressure field due to the $\epsilon(r)$ term. If the output sampling rate were near but not exactly an integral multiple of $2\pi/k_0$ the error term would include a low-frequency modulation from the $\sin k_0r$ term.

This kind of slowly varying error introduced by aliasing on this grid is difficult to distinguish from an accurate transform. We will show that samples on this grid can also be misleading when the Fourier–Bessel series is used to perform the transform, so that this phenomenon is not confined to the asymptotic implementation of the Hankel transform (see Fig. 23). We suspect that the importance of aliasing in the generation of synthetic fields has been obscured by the natural appearance of the $\pi n/k_0$ grid.

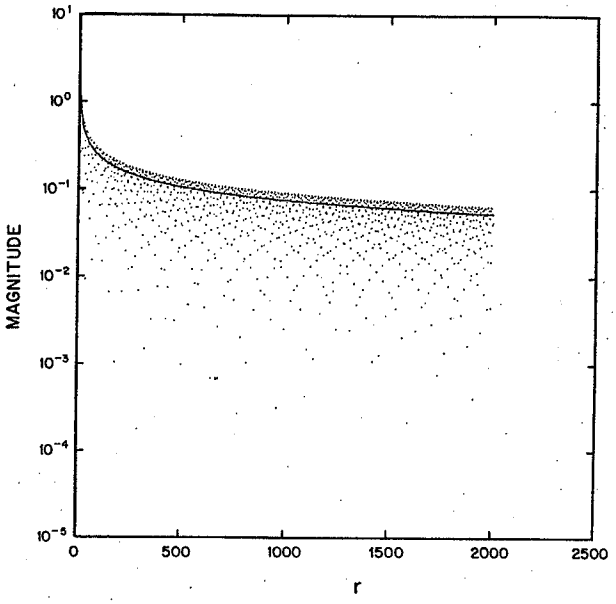

FIG. 4. Magnitude of the Hankel transform of a pole computed numerically (dots) compared with the exact result (solid curve).

B. Example 2

In this example we consider evaluation of the known integral

$$\int_0^\infty \frac{1}{k_r^2-\alpha^2}J_0(k_rr)k_r\,dk_r=\frac{-\pi i}{2}H_0^{(1)}(\alpha r),\quad \operatorname{Im}\alpha>0, \tag{24}$$

which decays roughly as $1/\sqrt{r}$ when $\operatorname{Im}\alpha$ is small. Poles such as this will appear in the Green's function when energy is guided in the radial direction by low speed layers. They may be present in the propagating portion of the spectrum when the top is included [$\Gamma_T(k_r)\neq 0$] and/or in the evanescent portion of the spectrum when low speed layers are present in the bottom, even for $\Gamma_T(k_r)=0$. They also arise when shear is included. The asymptotic $1/\sqrt{r}$ decay of the $H_0^{(1)}(\alpha r)$ is characteristic of the decay in two dimensions associated with such guided energy. Since the field decays asymptotically as $1/\sqrt{r}$, the replicated image of $\sqrt{r}P(r)$ does not decay at all. The replication will produce severe problems no matter what the sampling rate and the estimate for $P(r)$ will look like noise with a $1/\sqrt{r}$ envelope. Figure 4 shows the magnitude of the numerical transform of the pole together with the magnitude of its known transform. As with the last example the presumed "bandwidth" chosen was $A=2000$, and input values were included up to a value of 2. The pole was at $k_r=0.91$. The results are as expected.

III. A HYBRID NUMERICAL/ANALYTIC METHOD FOR COMPUTING SYNTHETIC FIELDS

In the previous section we showed that serious aliasing problems can occur when the Hankel transform is used to numerically generate fields that decay as slowly as $1/r$. In

this section we develop a method for computing synthetic fields, that significantly reduces aliasing problems by removing the $i/\sqrt{k_0^2 - k_r^2}$ singularity in the Green's function. We then extend this method to remove pole singularities in the Green's function associated with fields that decay as $1/\sqrt{r}$ due to perfectly trapped modes in the bottom. It is only necessary to remove those singularities that are close enough to the real k_r axis to disrupt the numerical evaluation of the Hankel transform. Unlike modal methods, the singularities not dealt with explicitly, have their contribution included in the numerical integration.

In order to implement the calculations, it is necessary to begin with the reflection coefficient for a plane wave in an isovelocity half-space incident upon a horizontally stratified bottom. In Appendix B we describe a technique for computing the reflection coefficient based on the Thomson–Haskell method[45,46] as it applies to a bottom consisting of a sequence of isovelocity, constant density layers, which may include absorption. The procedure we describe is numerically stable, even in the evanescent wave region where the solutions in each layer are growing and decaying exponentials. This stability is essential if the poles associated with trapped modes are to be properly computed but is often not present in algorithms intended to compute the reflection coefficient only for horizontal wavenumbers less than k_0. The discussion that follows assumes that the reflection coefficient has already been generated by this or some other technique.

A. Computing fields with no trapped modes

The asymptotics of a Hankel transform are determined by the singularities in the function to be transformed.[41] When there are no poles in the Green's function for real k_r (corresponding to no imbedded slow speed layers) then the $i/\sqrt{k_0^2 - k_r^2}$ singularity due to the source spectrum and the $\exp(i\sqrt{k_0^2 - k_r^2}\,|z + z_0|)$ migration term must dominate the asymptotic behavior of the field. The first of these gives rise to asymptotic $1/r$ decay as evidenced by the relation

$$\frac{e^{ik_0 r}}{r} = \int_0^\infty (i/\sqrt{k_0^2 - k_r^2})\, J_0(k_r r) k_r\, dk_r, \quad r > 0. \tag{25}$$

The migration term, $\exp(i\sqrt{k_0^2 - k_r^2}\,|z + z_0|)$, gives rise to asymptotic $1/r^2$ decay as evidenced by

$$(z + z_0)\exp\left[ik_0\sqrt{r^2 + (z + z_0)^2}\right]/[r^2 + (z + z_0)^2] = \int_0^\infty \exp(i\sqrt{k_0^2 - k_r^2}\,|z + z_0|)\, J_0(k_r r) k_r\, dk_r. \tag{26}$$

Because the $i/\sqrt{k_0^2 - k_r^2}$ singularity is responsible for the slow asymptotic $1/r$ decay, we can reduce the aliasing problem by following an established tradition in the asymptotic evaluation of integrals. We remove the singularity and determine its contribution analytically. We do so in a manner, however, that insures that the remaining portion of the integral has no singular behavior and can be performed numerically. Denoting P_R as the reflected pressure field and Γ as the bottom reflection coefficient, we rewrite

$$P_R(r) = \int_0^\infty \Gamma(k_r)(i/\sqrt{k_0^2 - k_r^2})\exp(i\sqrt{k_0^2 - k_r^2}\,|z + z_0|)\, J_0(k_r r) k_r\, dk_r, \tag{27}$$

as

$$P_R(r) = \int_0^\infty [\Gamma(k_r) - \Gamma(k_0)](i/\sqrt{k_0^2 - k_r^2})\exp(i\sqrt{k_0^2 - k_r^2}\,|z + z_0|)\, J_0(k_r r) k_r\, dk_r + \Gamma(k_0)\int_0^\infty (i/\sqrt{k_0^2 - k_r^2})\exp(i\sqrt{k_0^2 - k_r^2}\,|z + z_0|)\, J_0(k_r r) k_r\, dk_r. \tag{28}$$

If we define

$$L(k_r) \equiv [\Gamma(k_r) - \Gamma(k_0)](i/\sqrt{k_0^2 - k_r^2})\exp(i\sqrt{k_0^2 - k_r^2}\,|z + z_0|), \tag{29}$$

so that $L(k_r)$ does not have the $1/\sqrt{k_0^2 - k_r^2}$ singularity at $k_r = k_0$ (Ref. 47) then we can write Eq. (28) as

$$P_R(r) = \int_0^\infty L(k_r)\, J_0(k_r r) k_r\, dk_r + \Gamma(k_0)\exp\left[ik_0\sqrt{r^2 + (z + z_0)^2}\right]/\sqrt{r^2 + (z + z_0)^2}. \tag{30}$$

Because $L(k_r)$ does not have this singularity along the path of integration, the output of the numerical transform will decay at a rate faster than $1/r$. The asymptotic $1/r$ decay in the field, $P_R(r)$, is provided by the analytic term which can be recognized as the specular reflection when r is very large (glancing incidence). Because the numerically computed portion of the field decays faster than $1/r$, the nearfield region will be less degraded by aliasing than a direct computation of the $P_R(r)$. When aliasing does start to be a problem in the numerical field, the total field will be dominated by the analytic term, which is decaying more slowly in r. These observations are confirmed in the examples which follow. They illustrate the generation of synthetic pressure fields through the hybrid algorithm implied by Eq. (30). The integral is performed using the Fourier–Bessel series to implement the Hankel transform and the analytic expression is due to the singularity. The Fourier–Bessel series is chosen despite its slowness, because its properties are well understood. The parameters used in the next three examples are $A = 2000$, $k_0 = 0.8976$, $|z + z_0| = 2$, and the maximum $k_r = 2$.

1. Hard bottom

This is the degenerate example because for $\Gamma(k_r)$ constant, the entire transform is performed analytically. The

f = 220 Hz
$|z + z_0| = 2$ m
$k_0 = .8975979\ m^{-1}$

$C_0 = 1540$ m/s
$\rho_0 = 1$ g/cm^3
$C_1 = 1493.8$ m/s
$\rho_1 = 1.5$ g/cm^3

FIG. 5. Acoustic parameters for the slow bottom example.

result of the analytic transform was compared to the direct numerical transform in Fig. 3.

2. Slow bottom

Figure 5 shows the bottom parameters for this example. Figure 6 shows the result of the hybrid calculation (solid line) versus a direct numerical calculation. The improvement is dramatic. Figure 7 compares the hybrid field of Fig. 6, with its numerically generated component. As can be seen, the nearfield is in fact dominated by the numerically generated component. As range increases this numeric term begins to suffer from aliasing problems but the analytic term begins to dominate, minimizing the effect of aliasing on the computed field at large ranges.

3. Fast bottom

Figure 8 shows the parameters of the fast bottom for this example. Figure 9 shows the hybrid calculation versus the direct numerical calculation. Figure 10 presents the hybrid field and its numeric component. The improvements are similar to the fast bottom case.

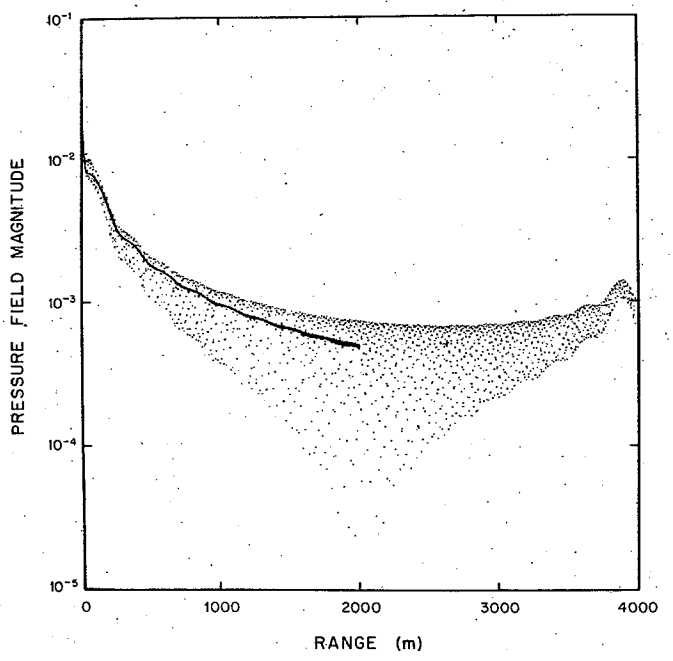

FIG. 6. Magnitude of field calculated using the hybrid method (solid curve) compared with a direct numerical calculation (dots) for the slow bottom example.

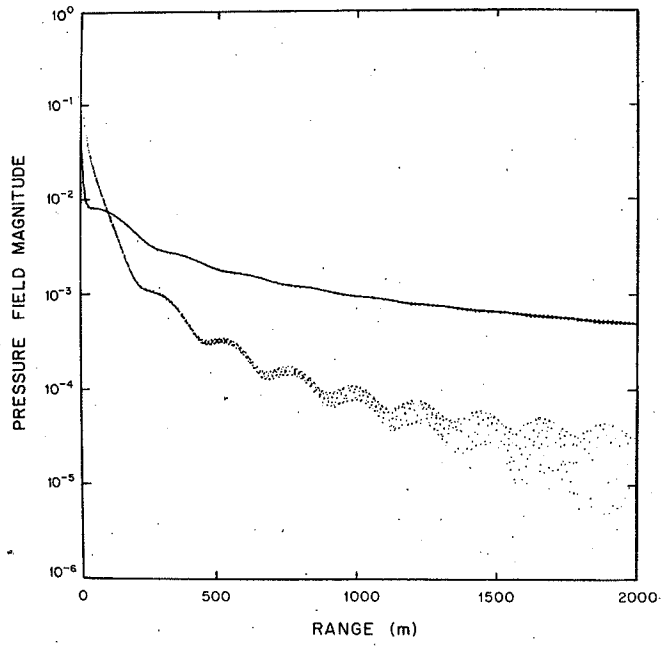

FIG. 7. Magnitude of hybrid field (solid curve) and its numerically generated component (dots) for the slow bottom example.

Removing the source singularity could also have been accomplished by transforming from horizontal wavenumber to angle. However, such a transformation would have sacrificed the form of the Hankel transform. By removing the singularity in the manner described, we have preserved the form of the Hankel transform and move smoothly into an asymptotic evaluation of the integral. Since $\Gamma(k_0) = -1$, this technique actually computes the variation of the field around the reflected field that would arise from a soft bottom. How quickly the asymptotics dominate is determined by how quickly the reflected field approaches this limit. In general the larger $z + z_0$ or the smaller the magnitude of $\Gamma(k_r)$, the longer the numerics will dominate. We will later discuss the generation of fields for $z + z_0$ large.

B. Computing fields with poles due to slow speed layers

Figure 11 shows the parameters of a slow speed layer between two isovelocity half-spaces. Figure 12 shows the magnitude and phase of the associated reflection coefficient, both for horizontal wavenumbers corresponding to real angles of incidence, $0 \leqslant \mathrm{Re}(k_r) \leqslant k_0$, and horizontal wavenumbers corresponding to complex angles of incidence,

f = 220 Hz
$|z + z_0| = 2$ m
$k_0 = .8975979\ m^{-1}$

$C_0 = 1540$ m/s
$\rho_0 = 1.0$ g/cm^3
$C_1 = 1700$ m/s
$\rho_1 = 2.0$ g/cm^3

FIG. 8. Acoustic parameters for the fast bottom example.

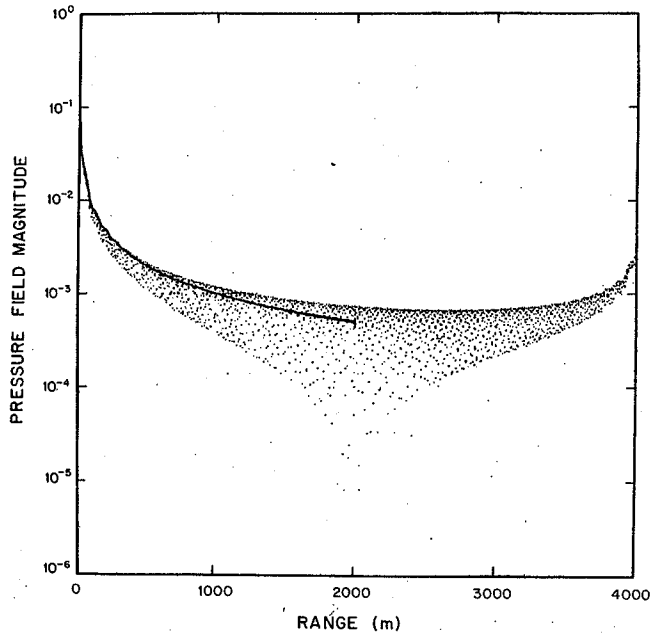

FIG. 9. Magnitude of field calculated using the hybrid method (solid curve) compared with a direct numerical calculation (dots) for the fast bottom example.

$\mathrm{Re}(k_r) > k_0$. We see that the reflection coefficient has an infinity in the evanescent wave region beyond k_0. This is due to a simple pole associated with a perfectly trapped mode excited in the low speed layer.[48] Since the mode is excited by tunneling via the evanescent part of the source spectrum, the infinity in the reflection coefficient does not violate conservation of energy.[49] Since the mode is constrained to propagate in the slow speed layer, which is acting as a waveguide, it decays in two dimensions rather than three and displays an

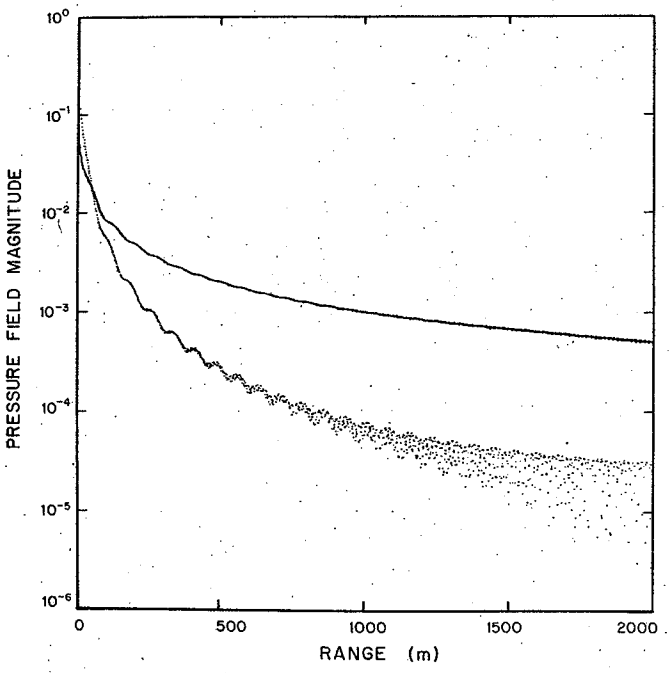

FIG. 10. Magnitude of hybrid field (solid curve) and its numerically generated component (dots) for the fast bottom example.

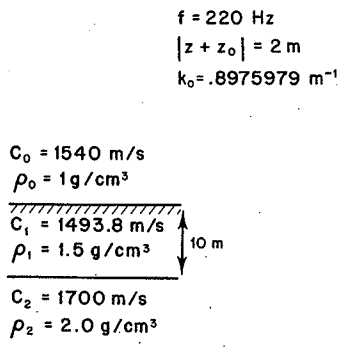

FIG. 11. Acoustic parameters for the slow speed layer example.

asymptotic decay of $1/\sqrt{r}$ characteristic of two-dimensional fields.

Poles such as this disrupt the asymptotic character of the field derived in the previous section. We would like to

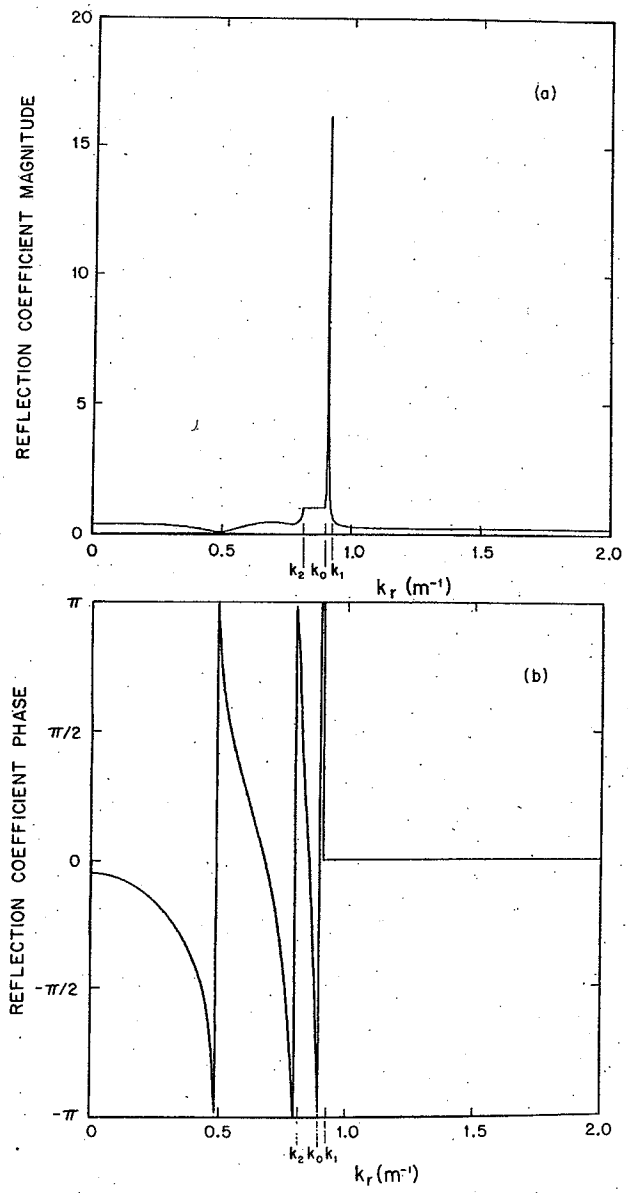

FIG. 12. Magnitude (a) and phase (b) of the reflection coefficient for the slow speed layer example.

analytically determine their contribution and remove them as we removed the $i/\sqrt{k_0^2 - k_r^2}$ singularity. To do so it is necessary to evaluate the integral

$$I(r, z+z_0; \alpha_i) \equiv \int_0^\infty (k_r^2 - \alpha_i^2)^{-1} (i/\sqrt{k_0^2 - k_r^2}) \times \exp(i\sqrt{k_0^2 - k_r^2}\,|z+z_0|)\, J_0(k_r r) k_r\, dk_r. \quad (31)$$

In Appendix D we show that for $\mathrm{Im}(\alpha_i) \geqslant 0$ (associated with no return from $r = \infty$) $I(r, z+z_0; \alpha_i)$ is given by

$$I(r, z+z_0; \alpha_i) = \frac{-1}{2\beta} \int_{-\infty}^{\infty} \frac{\exp(ik_0\sqrt{r^2+\xi^2})}{(r^2+\xi^2)^{1/2}} e^{-\beta|z+z_0-\xi|}\, d\xi - (i\pi/2\beta) H_0^{(1)}(\alpha_i r) e^{-\beta|z+z_0|}, \quad (32)$$

where β is defined as

$$\beta \equiv +\sqrt{\alpha_i^2 - k_0^2}. \quad (33)$$

The second term in Eq. (32) has the form of a conventional modal field. It has a logarithmic singularity as r approaches zero. This singularity is canceled by a logarithmic singularity in the first term at $r = 0$ when $z + z_0 \neq 0$. The total function $I(r, z+z_0; \alpha_i)$ is finite everywhere and can be computed accurately for all r. As such it is superior to the standard modal form as a representation for the pole contribution. For small values of r, $I(r, z+z_0; \alpha_i)$ is computed by expanding the integral in the first term asymptotically around its logarithmic singularity. The asymptotic expansion of the Hankel function in the second term around its logarithmic singularity is then used so that the two singularities cancel. For large ranges the first term rapidly approaches

$$\frac{-1}{2\beta^2} \frac{\exp[ik_0\sqrt{r^2+(z+z_0)^2}]}{[r^2+(z+z_0)^2]^{1/2}}, \quad (34)$$

which decays as $1/r$ and is eventually dominated by the $1/\sqrt{r}$ decay of the Hankel function in the second term. In intermediate ranges the first term can be easily evaluated by numerical integration.

With $I(r, z+z_0; \alpha_i)$ so defined, the reflected pressure field can be written as

$$P_R(r) = \int_0^\infty \frac{i}{(k_0^2 - k_r^2)^{1/2}} \left(\Gamma(k_r) - \sum_i \frac{a_i}{k_r^2 - \alpha_i^2} \right) \times \exp(i\sqrt{k_0^2 - k_r^2}\,|z+z_0|)\, J_0(k_r r) k_r\, dk_r + \sum_i a_i I(r, z+z_0; \alpha_i), \quad (35)$$

where the expression in large parentheses no longer has any poles near the line of integration and so can be evaluated as before.

Equations (32) and (35) are correct for $\mathrm{Im}(\alpha_i) > 0$, and poles off axis could in principle be removed in this manner as well. However, when $\mathrm{Im}(\alpha_i) \gg 0$ the poles no longer contribute asymptotically as $1/\sqrt{r}$ because the Hankel function decays exponentially. Under these conditions the asymptotic form of the Hankel function becomes

$$H_0^{(1)}(\alpha_i r) \approx \sqrt{2/(\pi\alpha_i r)}\, e^{i(\alpha_i r - \pi/4)} = \sqrt{2/(\pi\alpha_i r)}\, e^{-\alpha_i'' r} e^{i\alpha_i' r} e^{-i\pi/4}. \quad (36)$$

As $\mathrm{Im}(\alpha_i)$ becomes large, the exponential decay dominates the $1/\sqrt{r}$ decay even over the finite range that concerns us and single off-axis poles do not contribute significantly to the asymptotics of the field. This coupled with the fact that it is difficult to determine the location of the off-axis poles accurately accounts for the fact that we remove only those poles near the real axis (close to the path of integration) and leave the others to the numerical part of the transform.

In order to remove the poles as required in Eq. (35) it is necessary to determine with precision the pole locations α_i and their scales a_i. The pole locations can be found using standard complex root finding techniques, though care must

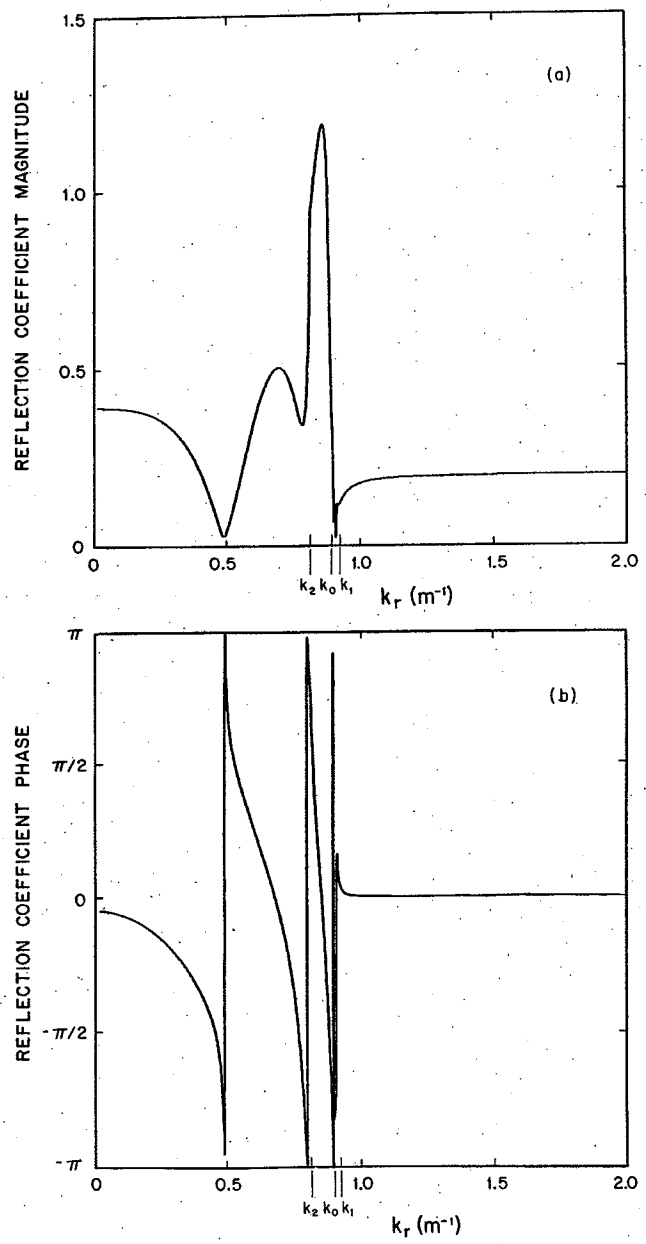

FIG. 13. Magnitude (a) and phase (b) of the reflection coefficient after the pole has been removed for the slow speed layer example.

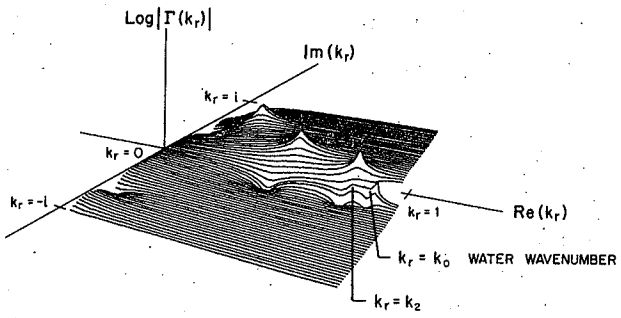

FIG. 14. Perspective plot of the log magnitude of the reflection coefficient for the slow speed layer example.

be taken to provide the root finding algorithm with values of the reflection coefficient on the Riemman surface so that it appears analytic except at isolated singularities. This means that the branches chosen for the square roots must be taken in such a manner that a branch cut is never placed between points used simultaneously in a calculation by the root finder. Once the root locations are known, the scale factors can be found for those singularities far from any others by determining a least squares fit to

$$\Gamma(k_{r_j}) = a_i/(k_{r_j}^2 - \alpha_i^2), \quad j = 1,2,..., N, \tag{37}$$

provided that the k_{r_j} are taken sufficiently close to α_i that $\Gamma(k_r)$ is well approximated by just one pole in that region.

If many poles are clustered together, they can be determined simultaneously by solving:

$$\Gamma(k_{r_j}) = \sum_{i \in I} \frac{a_i}{k_{r_j}^2 - \alpha_i^2}, \quad j = 1,2,..., N, \tag{38}$$

for N sufficiently large. If a pole is near a branch cut then the poles on the other side of the cut, on the opposite sheet, and near the cut must also be considered to be near that pole. Other techniques for finding or improving estimates of the pole locations include the Rayleigh–Ritz method.[2]

Figure 13(a) and (b) shows the magnitude and phase of the reflection coefficient of Fig. 12 minus the pole contribution:

$$\Gamma(k_r) - a/(k_r^2 - \alpha^2). \tag{39}$$

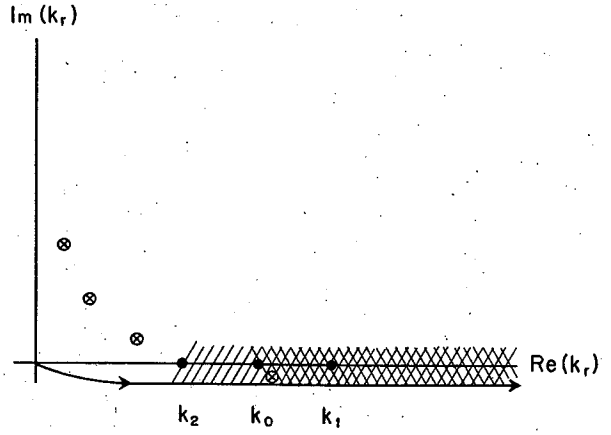

FIG. 15. Schematic illustration of poles, branch cuts, and integration path in the complex k_r plane for the slow speed layer example.

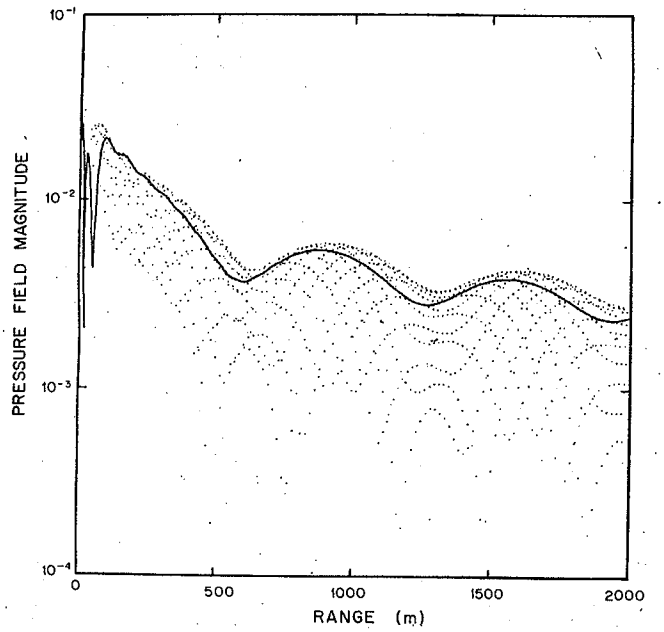

FIG. 16. Magnitude of field calculated using the hybrid method with pole removal (solid curve) compared with field calculated without pole removal (dots) for the slow speed layer example.

For this example $a = 1.689712\times10^{-2} + i5.027826\times10^{-4}$ and $\alpha = 9.069830\times10^{-1} + i2.488749\times10^{-5}$.

Note the difference in scale between Figs. 12(a) and 13(a). The small notch visible at $k_r \approx \alpha_i$ is probably due to a small amount of error in the estimate of α_i.

A notable feature of Fig. 13(a) is an unmasking of off-axis poles and zeros, particularly in the region $k_2 < k_r < k_0$ where previously $|\Gamma(k_r)| = 1$. These can be clearly seen in the perspective plot of the log magnitude of the total reflection coefficient in the complex plane presented in Fig. 14 for

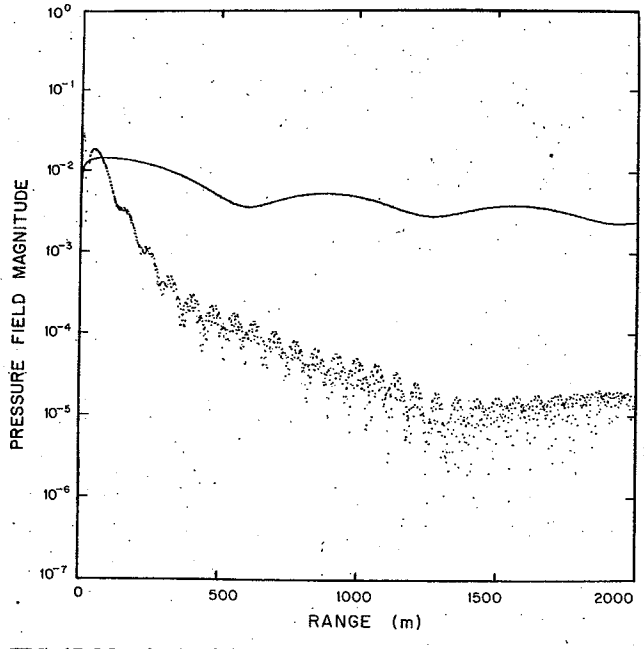

FIG. 17. Magnitude of the analytically generated pole contribution (solid curve) and the remainder of the field exclusive of the pole contribution (dots) for the slow speed layer example.

the sheet $\mathrm{Re}(\sqrt{k_0^2 - k_r^2}) > 0$ and $\mathrm{Re}(\sqrt{k_2^2 - k_r^2}) > 0$ corresponding to positive real power flow for the incident and transmitted waves. A discontinuity extends from k_2 along the real k_r axis to infinity, corresponding to the branch cut extending from the branch point at k_2. Another cut extending from k_0 to infinity falls on this same line and is therefore not apparent. In addition to the pole on the real k_r axis, other off-axis poles corresponding to leaky modes are also apparent in the reflection coefficient. In Fig. 15, we present a more conventional plot illustrating schematically the branch cuts and pole positions along with the choice of integration path along which $\mathrm{Im}(\sqrt{k_0^2 - k_r^2}) > 0$ and $\mathrm{Im}(\sqrt{k_2^2 - k_r^2}) > 0$, thus guaranteeing convergence of the fields at infinity.

Figure 16 presents the hybrid field (solid line) versus the field calculated without removing the pole from the reflection coefficient (but otherwise removing the $1/\sqrt{k_0^2 - k_r^2}$ singularity as in the previous hybrid examples). The parameters used in the Fourier–Bessel series were $A = 2000$ and maximum $k_r = 2$. The spread in the directly computed field due to aliasing is severe as predicted for a function that decays as $1/\sqrt{r}$. The hybrid field does not exactly follow the contour of the top of the spread just as the hybrid computations in the previous examples did not exactly follow those contours when the aliasing became severe. Figure 17 presents the magnitude for the analytically generated pole contribution (solid line) and the remainder of the field exclusive of the pole contribution. The nonpole contribution is most significant for short ranges, while for this near bottom geometry the pole contribution dominates farther out.

The expression for $I(r, z + z_0; \alpha_i)$ in Eq. (32) shows that the contribution of the pole to the field decreases exponentially with $|z + z_0|$. In this example $|z + z_0| = 2$ m to emphasize the nearfield behavior associated with the pole. For larger values of $|z + z_0|$ the pole contribution would be considerably less. Equation (32) can be used to estimate the magnitude of the pole contribution if the pole location α_i and $|z + z_0|$ are known.

IV. LARGE SOURCE–RECEIVER HEIGHTS

In the previous section we described a hybrid method for calculating synthetic pressure fields. In the absence of poles, the analytic contribution was given by

$$\Gamma(k_0)\exp[ik_0\sqrt{r^2 + (z + z_0)^2}]/\sqrt{r^2 + (z + z_0)^2}, \quad (40)$$

which dominates the reflected field as r approaches infinity. In general, $\Gamma(k_0) = -1$. Consequently, the analytic contribution corresponds to the field that would have been generated by a perfect (soft) reflector. In the absence of poles, this is the field that will be seen at very large offsets. The numerical calculations provide the variation around this asymptotic expression for the field. The method is most useful when the asymptotics dominate quickly. We have found that for large $z + z_0$, larger offsets are required to reach the point where the asymptotics dominate. This is intuitively reasonable since larger offsets are then required to achieve the same degree of grazing. For such a case, the hybrid procedure described in the last section still improves the accuracy of field calculations but a fast, efficient method for calculating the numerical Hankel transform is also required because the numerical transform must be accurate to a larger range.

An efficient method for evaluating the Hankel transform has recently been described in the literature.[21,7] This procedure calculates the Hankel transform of a function by first numerically computing its Abel transform. When a Fourier transform is applied to the result, the Hankel transform of the original function is obtained. The numerical procedure for performing the Abel transform implements that transform of a function, $\tilde{G}(k_r)$, as a convolution of the function $G(k_r)$ defined as

$$\tilde{G}(k_r) \equiv G(\sqrt{|k_r|}). \quad (41)$$

The convolution is implemented using an FFT with care taken to properly handle a singularity that arises in the integrand that would otherwise lead to aliasing problems. The Abel transform algorithm (and consequently the Hankel transform algorithm) works well provided that the input function, $G(k_r)$ is well represented on the grid $\sqrt{nT}$ with $n = 0,1,2,\ldots$. On such a grid, the spacing between samples is given by $\sqrt{(n+1)T} - \sqrt{nT} \approx 2^{-1}\sqrt{T/n}$ where T is the sampling period. Functions with moderate increases in complexity with k_r are better represented on such a grid than on an even grid. The plane-wave reflection coefficient and the Green's function are examples of such functions. The magnitude and phase plots of the reflection coefficients discussed in this paper are typical of these functions. They show that $\Gamma(k_r)$ (and consequently the Green's function as well) have increasing rates of change with k_r. Consequently, this fast Hankel transform method works very well for the generation of synthetic fields.

We now present a realistic example with parameters that are typical of the deep ocean,[9,11] as shown in Fig. 18. The sum of the source and receiver heights for this example is large, making it necessary to use the efficient algorithm just described. We assume a pseudolinear sound speed profile in a sediment layer of thickness h so that

$$1/c^2(z) = [1/c_1^2(z)](1 - \beta z), \quad z > 0, \quad (42)$$

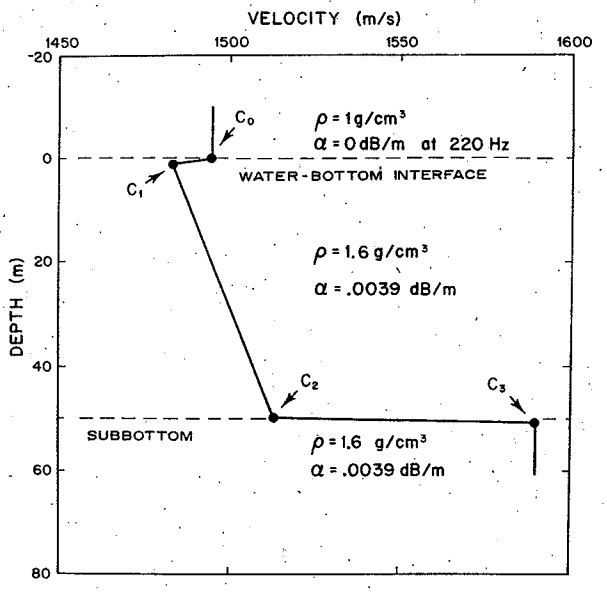

FIG. 18. Acoustic parameters for the realistic ocean bottom example.

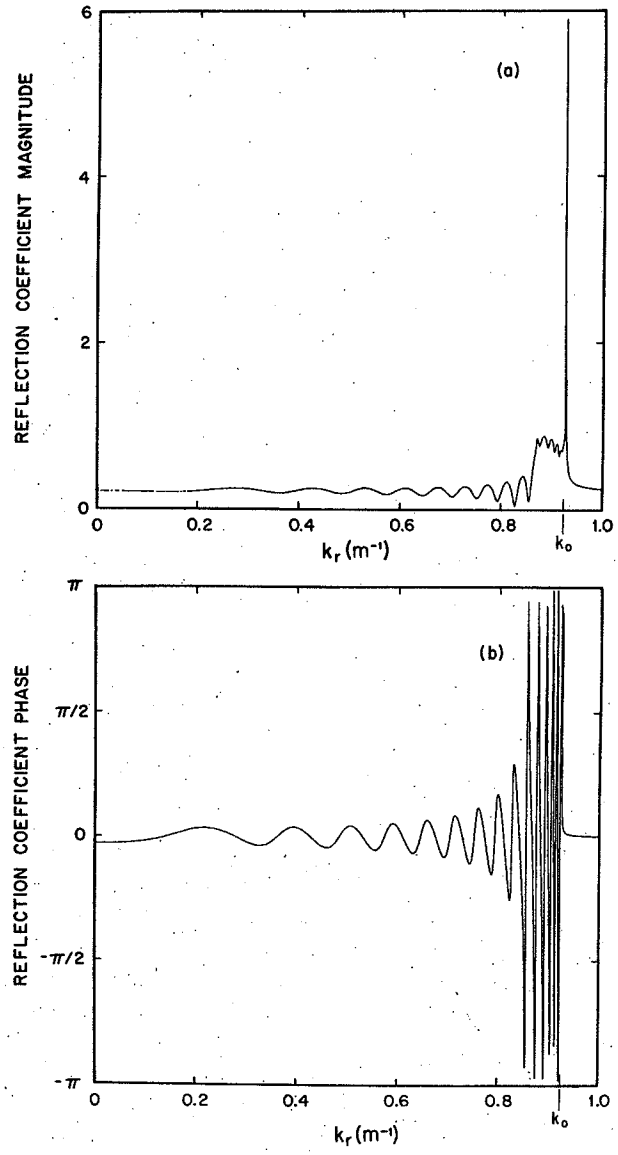

FIG. 19. Magnitude (a) and phase (b) of the reflection coefficient for the realistic bottom example.

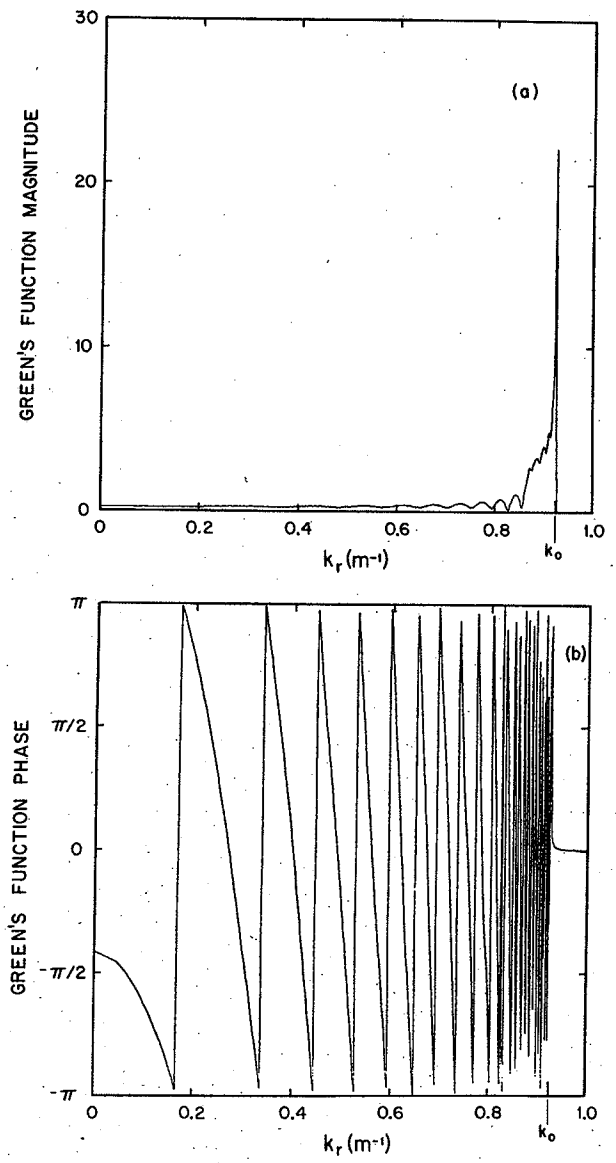

FIG. 20. Magnitude (a) and phase (b) of the Green's function for the realistic bottom example.

where

$$\beta = (1/h)(1 - c_1^2/c_2^2). \tag{43}$$

The specific values used are $c_0 = 1495$ m/s, $c_1 = 1483.339$ m/s, $c_2 = 1513.719$ m/s, $c_3 = 1590$ m/s, and $h = 50$ m. This profile was approximated by 50 isovelocity layers and the reflection coefficient computed using the procedure described in Appendix B. Figure 19 presents the reflection coefficient for this example, while Fig. 20 presents the Green's function. In Fig. 21, we show the magnitude of the reflected pressure field together with the magnitude of the analytic component of the calculation, for $z_0 = 124.94$ m and $z = 1.17$ m. For this geometry, the pole contribution is negligible and does not need to be removed. The computation was carried out to a range of 25 736 m in order to minimize the aliasing effects over the ranges of interest. The numerical contribution took about 1 min on a VAX-11/780. To achieve a comparable accuracy, about 8 h would have been required if the Fourier–Bessel series had been used.

Figure 22 shows the total field, obtained by adding the source field $e^{ik_0R_0}/R_0$ to the computed reflected field, where $R_0 \equiv \sqrt{r^2 + (z - z_0)^2}$. Also shown is a synthetic field calculated for the same case using a ray method developed by Bartberger and described in the references of Ref. 11. The ray method contains a phase correction, but no amplitude correction, in caustic regions. Because this field is generated by such a completely different method, the close correspondence between the two fields is a strong indication of the validity of our procedure. The only appreciable discrepancy occurs in a caustic region where, as mentioned, this ray method is known to be inaccurate.

Figure 23 shows the magnitude of this field generated using the Fourier–Bessel series (with $A = 6000$ m and maximum $k_r = k_0$), where the Green's function has been inadequate, sampled together with the magnitude of the field generated using the Hankel–Abel program. The output of the Fourier–Bessel series is shown on the set of samples $\pi n/k_0$ for $n = 0,1,2,\ldots, N/2$, which is the set that would have result-

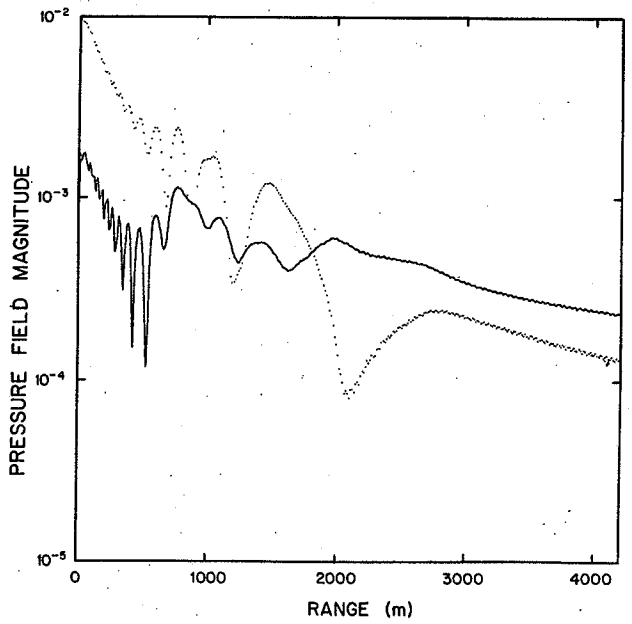

FIG. 21. Magnitude of reflected pressure field calculated with the hybrid method (solid curve) and its analytic component (dots) for the realistic bottom example.

ed if an FFT were used to approximately evaluate the Hankel transform and values of the Green's function were used exactly up to the water wavenumber k_0. A comparison of the output of the Fourier–Bessel series with the correct field shows that it is slightly offset, that the farthest null (in range) is insufficiently deep and the tail has the wrong slope. These effects are due to aliasing as was discussed in Sec. II and appear as smooth errors because of the sampling grid chosen for the display. Without an adequate understanding of the effects of aliasing, this curve might have been accepted as a correct representation of the field. It has been included to underscore the subtle effects possible from aliasing.

V. CONCLUSION

We have presented a hybrid numerical/analytical technique for computing the field due to a point source in a stratified medium. This technique is based upon the exact Hankel transform relationship between the field in the range domain and the depth-dependent Green's function in the horizontal wavenumber domain. The approach was basically numerical in nature, as the discrete implementation of the Hankel transform was viewed and treated in a manner analogous to the discrete implementation of the Fourier transform. Within this context, sampling was identified as the major source of error, and it was shown that severe aliasing errors can arise in computed fields due to undersampling at infinities of the Green's function. Aliasing results were derived using both the asymptotic and Fourier–Bessel series Hankel transform algorithms. It was shown that the aliasing errors could be substantially reduced by removing the infinities and computing their contribution to the field analytically. The resultant procedure is one in which, in principle, the sum of the numerical and analytic parts always equals the true field. Unlike standard modal methods, the two parts are finite even at zero range, and explicit branch line integrals do not appear. The technique includes the evanescent portion of the Green's function and accurately generates the effects due to trapped modes. The trapped modes can dominate the field for large offsets because of their slow asymptotic decay. The method is accurate both in the near- and farfields.

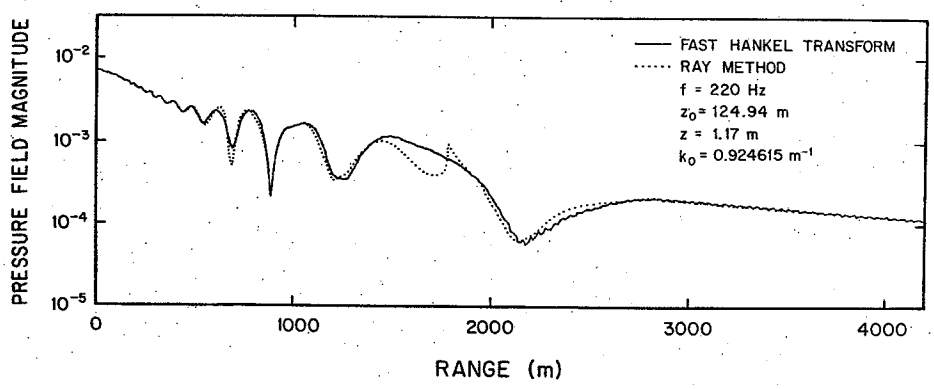

FIG. 22. Magnitude of total hybrid field including source field (solid curve) compared with results from a ray method (dots).

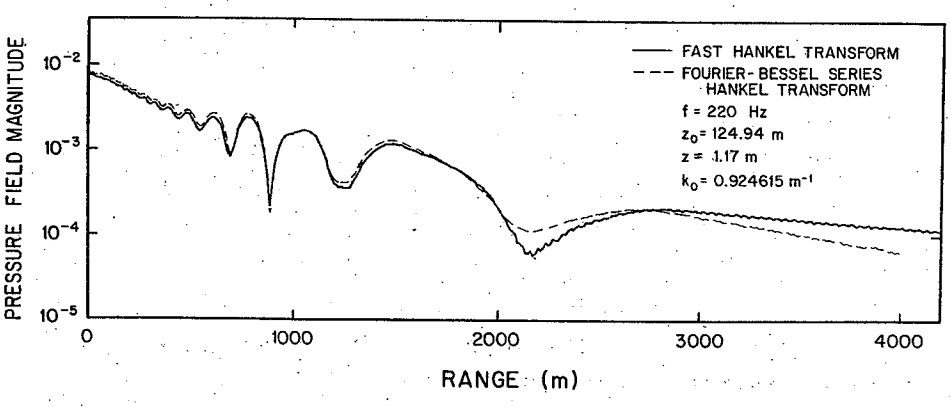

FIG. 23. Magnitude of total hybrid field calculated using the fast Hankel transform algorithm (solid curve) and the Fourier–Bessel series (dashes).

The method was developed in detail for the acoustics problem of a monochromatic point source and receiver in an isovelocity fluid half-space overlying a horizontally stratified fluid medium. It was found that under circumstances of interest in ocean bottom acoustics, where the Green's function consists of a finite continuum with a few infinities to be removed, the technique is effective, efficient, and extremely accurate. It was demonstrated for a hard bottom and a slow and fast isovelocity bottom examples using the Fourier–Bessel series. A new fast Hankel transform algorithm was used to generate synthetic data for a realistic ocean bottom acoustic sound speed profile and experimental geometry. The results were shown to be in excellent agreement with those from a conventional ray technique in those regions where the ray technique is believed to be accurate.

ACKNOWLEDGMENTS

The authors are grateful to David Stickler of the Courant Institute of Mathematical Sciences, New York University, for useful comments, and James Doutt for helpful discussion and programming assistance. They are grateful to Michael Wengrovitz for implementing the fast Hankel transform algorithm on the computer for this problem. This work was supported in part by ONR Contract N00014-82-C-0152 at WHOI, and in part at MIT by the Advanced Research Projects Agency, monitored by ONR under Contract N00014-81-K-0742-NR-049-506, and the National Science Foundation under grant ECS80-07102, and by Sanders Associates, Inc. This paper is Woods Hole Oceanographic Institution Contribution No. 5453.

APPENDIX A: SAMPLING AND ALIASING FOR THE FOURIER–BESSEL SERIES

In this appendix we examine the form that aliasing takes for the Hankel transform when it is evaluated using the Fourier–Bessel series. We derive an expression that relates the output of the Fourier–Bessel series to the true Hankel transform. Because the Fourier–Bessel series uses samples on a set of points that is approximately evenly spaced, the results we derive will be approximately correct for any evenly spaced sampling scheme.

We begin with the formulation of the Fourier–Bessel series[24,25] which states[50]:

$$0<r<1, \quad P(r)=2\sum_{n=1}^{\infty}\int_0^1 \frac{P(\xi)\,J_0(\lambda_n\xi)\xi\,d\xi}{J_1^2(\lambda_n)}J_0(\lambda_n r), \tag{A1}$$

where λ_n, $n=1,2,3,\ldots$ are the ordered zeros of $J_0(\cdot)$.

If $P(r)=0$ for $r>1$ then the integral in the expression above is just the Hankel transform of $P(r)$ evaluated at λ_n, $G(\lambda_n)$, so that the Hankel transform $P(r)$ can be expressed exactly as a sum:

$$0<r<1, \quad P(r)=2\sum_{n=1}^{\infty}\frac{G(\lambda_n)}{J_1^2(\lambda_n)}J_0(\lambda_n r)$$

$$\text{when } P(r)=0 \text{ for } r>1. \tag{A2}$$

When $P(r)$ is not truly bandlimited to $r<1$ and/or the sum is not carried out to infinity, Eq. (A2) is only an approximation to the Hankel transform. We have considered the effect of carrying the sum only out to a finite value when we considered the effect of windowing in the body of this paper. Here we consider only the degradation that occurs because the infinite series is used in place of the integral. Finally, we note that it is because the zeros of $J_0(\cdot)$, λ_n, rapidly approach $n\pi-\frac{1}{4}$ that the sampling above is approximately evenly spaced.

To determine the effect of approximating the Hankel transform:

$$P(r)=\int_0^{\infty} G(k_r)\,J_0(k_r r)k_r\,dk_r, \tag{A3}$$

by the Fourier–Bessel series:

$$0<r<1, \quad \hat{P}(r)=\sum_{n=1}^{N}\frac{2}{J_1^2(\lambda_n)}G(\lambda_n)\,J_0(\lambda_n r), \tag{A4}$$

we express $\hat{P}(r)$ in terms of the correct transform, $P(r)$, by inverting (A3) to write $G(k_r)$ in terms of $P(r)$. We substitute this into Eq. (A4) to yield

$0<r<1$,

$$\hat{P}(r)=\sum_{n=1}^{N}\frac{2}{J_1^2(\lambda_n)}\left(\int_0^{\infty}P(\xi)\,J_0(\lambda_n\xi)\xi\,d\xi\right)J_0(\lambda_n r). \tag{A5}$$

Interchanging the order of integration and summation we have

$$\hat{P}(r)=\int_0^{\infty}P(\xi)T_N(r,\xi)\xi\,d\xi, \tag{A6}$$

where, following the notation of Watson[24] we define

$$T_N(r,\xi)\equiv 2\sum_{n=1}^{N}\left(\frac{J_0(\lambda_n\xi)\,J_0(\lambda_n r)}{J_1^2(\lambda_n)}\right). \tag{A7}$$

The effect of aliasing is summarized by $T_\infty(r,\xi)$. We can obtain an expression for $T_\infty(r,\xi)$ by using an asymptotic result presented by Schlafli[51–53]:

$$T_N(r,\xi)\to(2\sqrt{r\xi})^{-1}\left(\frac{\sin A_N(r-\xi)}{\sin(\pi/2)(r-\xi)}-\frac{\sin A_N(2-r-\xi)}{\sin\,[\pi(2-r-\xi)/2]}\right), \tag{A8}$$

where $A_N\equiv(N+\frac{1}{4})\pi$. As N approaches infinity $T_N(r,\xi)$ approaches a weighted sequence of impulses. We determine that sequence here.

To determine the limit of the expression in Eq. (A8) we first consider the expression

$$\frac{\sin A_N x}{\sin(\pi x/2)}=\frac{\sin(N\pi x+\pi x/4)}{\sin(\pi x/2)}, \tag{A9}$$

which equals

$$\frac{\sin N\pi x}{\sin(\pi x/2)}\cos\frac{\pi x}{4}+\frac{\cos N\pi x}{\sin(\pi x/2)}\sin\frac{\pi x}{4}. \tag{A10}$$

As $N\to\infty$ the first term in (A10) approaches the limit

$$\sum_k(-1)^k\delta(x/2-2k). \tag{A11}$$

The second term in Eq. (A10) approaches 0 (Ref. 54). The limit of Eq. (A9) is therefore given by

$$\lim_{N\to\infty}\frac{\sin A_N x}{\sin(\pi x/2)}=\sum_k(-1)^k\delta\left(\frac{x}{2}-2k\right). \tag{A12}$$

Using Eq. (A12) the first term in Eq. (A8) can now be seen to approach the limit

$$\lim_{N\to\infty}\frac{\sin A_N(r-\xi)}{\sin[\pi(r-\xi)/2]}=2\sum_k(-1)^k\delta(r-\xi-4k). \tag{A13}$$

The second term in Eq. (A8) can be put in the form of Eq. (A9) by defining $y\equiv 2-r-\xi$,

$$\frac{\sin A_N(2-r-\xi)}{\sin[\pi(2-r-\xi)/2]}=\frac{\sin A_N y}{\sin(\pi y/2)}. \tag{A14}$$

Combining Eqs. (A13) and (A14) we have

$$\lim_{N\to\infty}\frac{\sin A_N(2-r-\xi)}{\sin[\pi(2-r-\xi)/2]}=2\sum_k(-1)^k\delta(2-r-\xi-4k). \tag{A15}$$

We can determine $T_\infty(r,\xi)$ by combining (A13) and (A15):

$$\lim_{N\to\infty}T_N(r,\xi)=(1/\sqrt{r\xi})\sum_k(-1)^k[\delta(r-\xi-4k)-\delta(2-r-\xi-4k)]. \tag{A16}$$

If our transform is not severely aliased so that $P(r)$ is negligible for $r>2$ then substituting Eq. (A16) into Eq. (A6) shows that

$0<r<1$,

$$\hat{P}(r)\approx\int_0^2 P(\xi)(1/\sqrt{r\xi})[\delta(r-\xi)-\delta(2-r-\xi)]\xi\,d\xi \tag{A17}$$

which equals for $0<r<1$ (Ref. 55):

$$\hat{P}(r)=P(r)-(\sqrt{2-r}/\sqrt{r})P(2-r). \tag{A18}$$

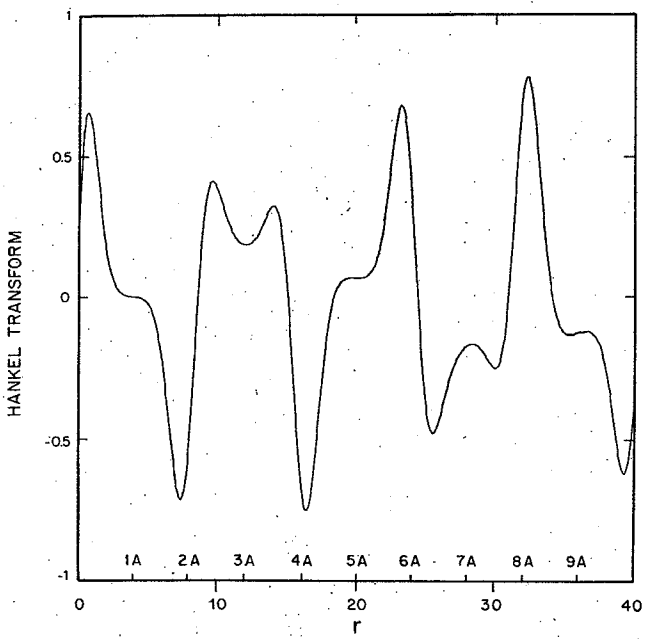

FIG. A1. Magnitude of $4\sqrt{r}$ · Hankel transform ($e^{-k^2/2}$) generated numerically using the Fourier–Bessel series.

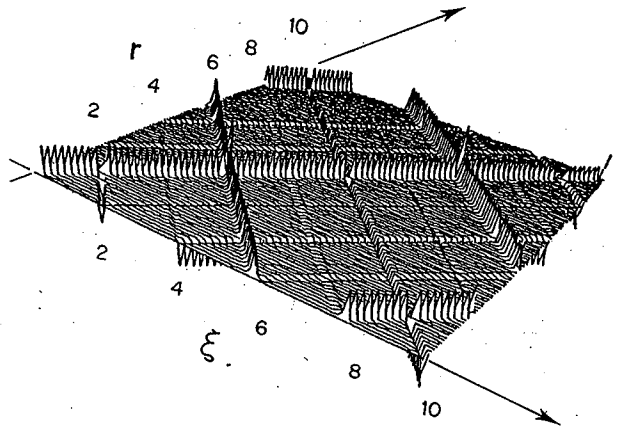

FIG. A2. Magnitude of $2\sqrt{r\xi}\,T_{128}(r,\xi)$.

We observe that the aliasing result most directly relates $\sqrt{r}\hat{P}(r)$ to $\sqrt{r}P(r)$.

An example of aliasing is presented in Fig. A1 where we see $\sqrt{r}$ times the Hankel transform of $e^{-k^2/2}$ generated with the Fourier–Bessel series. The bandwidth A assumed was 4. The figure displays the aliasing terms generated by the impulses in Eq. (A16). In the region $0<r<2A$ the figure matches the result indicated in Eq. (A17) very well. In the region $2A<r<4A$ the figure does not correspond exactly to what would be determined by substitution of Eq. (A16) into Eq. (A6) indicating the limited validity of Schlafli's result.

Figure A2 shows a plot of $2\sqrt{r\xi}\,T_{128}(r,\xi)$ $0<r<10$, $0<\xi<10$. This picture supports the accuracy of Eq. (A16) for $T_\infty(r,\xi)$ for $0<r+\xi\leqslant 2A$ and suggests that Eq. (A16) is at least approximately correct over the range of r and ξ shown in the figure.

APPENDIX B: GENERATING THE PLANE-WAVE REFLECTION COEFFICIENT

In this appendix we develop a numerical implementation of the propagator matrix method for generating the plane-wave reflection coefficient that is well behaved numerically, even in the evanescent wave region. We begin by describing the computation of the plane-wave reflection coefficient by means of the Thomson–Haskell method as it applies to a sequence of isovelocity, constant density layers.[45,46] The wavenumber in each layer may be complex, thereby accommodating absorption.

A. The method in principle

1. Overview

To calculate the plane-wave reflection coefficient we consider the response of a layered bottom to an incident plane wave as shown in Fig. B1. Within the nth isovelocity layer we express the field as the vector

$$\begin{bmatrix}P(z)\\U(z)\end{bmatrix}_n J_0(k_r r)e^{-i\omega t}, \tag{B1}$$

where $P_n(z)$ is the pressure in the nth layer and $U_n(z)$ is the

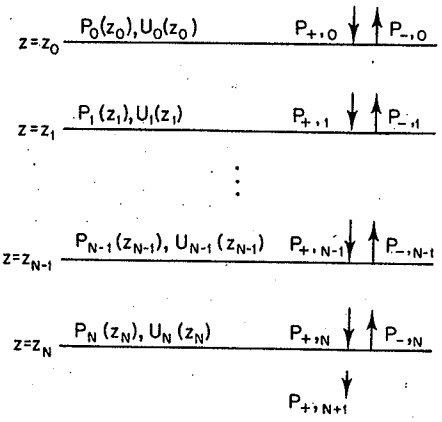

FIG. B1. Isovelocity layered bottom model used in reflection coefficient calculations.

normal component of the velocity. We have chosen this representation because $P(z)$ and $U(z)$ are continuous in z, even across layer interfaces. In the discussion which follows we will suppress the time and radial dependence of the field because they are the same in all layers.

In the propagator matrix approach, the admittance (inverse impedance) at the bottom layer is the characteristic admittance at oblique incidence because of the isovelocity half-space termination:

$$Y_{N+1} \equiv U(z_{N+1})/P(z_{N+1}). \tag{B2}$$

This characteristic admittance at oblique incidence is available from the material parameters. In principle it is used to determine the reflection coefficient at the top interface in three steps. First the field at the top interface is related to the field at the bottom interface by the propagator matrix:

$$\begin{bmatrix} P(z_0) \\ U(z_0) \end{bmatrix} = \Phi \begin{bmatrix} P(z_N) \\ U(z_N) \end{bmatrix}. \tag{B3}$$

Next the incident and reflected pressure waves at the surface are related to the field at the top interface and then to those at the bottom through:

$$\begin{bmatrix} P_{+,0} \\ P_{-,0} \end{bmatrix} = A \begin{bmatrix} P(z_0) \\ U(z_0) \end{bmatrix} = A\Phi \begin{bmatrix} P(z_N) \\ U(z_N) \end{bmatrix} \equiv \begin{bmatrix} \alpha_{11} & \alpha_{12} \\ \alpha_{21} & \alpha_{22} \end{bmatrix} \begin{bmatrix} P(z_N) \\ U(z_N) \end{bmatrix}. \tag{B4}$$

Finally, the reflection coefficient is calculated in terms of the admittance, Y_{N+1}, using

$$\begin{bmatrix} P_{+,0} \\ P_{-,0} \end{bmatrix} = \begin{bmatrix} \alpha_{11} & \alpha_{12} \\ \alpha_{21} & \alpha_{22} \end{bmatrix} \begin{bmatrix} 1 \\ Y_{N+1} \end{bmatrix} P(z_{N+1}), \tag{B5}$$

so that

$$\Gamma = \frac{P_{-,0}}{P_{+,0}} = \frac{\alpha_{21} + Y_{N+1}\alpha_{22}}{\alpha_{11} + Y_{N+1}\alpha_{12}}. \tag{B6}$$

2. The propagator matrix

The essential element of this approach is the propagator matrix, Φ, of Eq. (B3). In this section we review its derivation.

Within any isovelocity layer, the field can be considered as the superposition of a positive and a negative traveling wave. The pressure field is given by

$$P(z) = P_+ e^{ik_z z} + P_- e^{-ik_z z}. \tag{B7}$$

The normal component of velocity, $U(z)$, is related to $P(z)$ through the telegraph equations.[56] For the non-normal case we use

$$-\frac{\partial P}{\partial z} = \rho \frac{\partial U}{\partial t} = -i\omega\rho U,$$

which implies that

$$U(z) = \frac{ik_z}{i\omega\rho} P_+ e^{ik_z z} - \frac{ik_z}{i\omega\rho} P_- e^{-ik_z z}, \tag{B8}$$

or defining the admittance $Y \equiv k_z/\omega\rho$,

$$U(z) = YP_+ e^{ik_z z} - YP_- e^{-ik_z z}. \tag{B9}$$

In matrix form Eqs. (B7) and (B9) become

$$\begin{bmatrix} P(z) \\ U(z) \end{bmatrix} = \begin{bmatrix} e^{ik_z z} & e^{-ik_z z} \\ Ye^{ik_z z} & -Ye^{-ik_z z} \end{bmatrix} \begin{bmatrix} P_+ \\ P_- \end{bmatrix}. \tag{B10}$$

If $\left[\begin{smallmatrix} P(z_1) \\ U(z_1) \end{smallmatrix}\right]$ is known at some point in the layer then $\left[\begin{smallmatrix} P(z_2) \\ U(z_2) \end{smallmatrix}\right]$ can be computed in principle by inverting Eq. (B10) to find $\left[\begin{smallmatrix} P_+ \\ P_- \end{smallmatrix}\right]$ in terms of $\left[\begin{smallmatrix} P(z_1) \\ U(z_1) \end{smallmatrix}\right]$ and then calculating $\left[\begin{smallmatrix} P(z_2) \\ U(z_2) \end{smallmatrix}\right]$ from $\left[\begin{smallmatrix} P_+ \\ P_- \end{smallmatrix}\right]$. Combining these operations into one step gives

$$\begin{bmatrix} P(z_2) \\ U(z_2) \end{bmatrix} = \begin{bmatrix} e^{-ik_z z_2} & e^{-ik_z z_2} \\ Ye^{ik_z z_2} & -Ye^{-ik_z z_2} \end{bmatrix} \times \begin{bmatrix} e^{ik_z z_1} & e^{-ik_z z_1} \\ Ye^{ik_z z_1} & -Ye^{-ik_z z_1} \end{bmatrix}^{-1} \begin{bmatrix} P(z_1) \\ U(z_1) \end{bmatrix}, \tag{B11}$$

which leads to

$$\begin{bmatrix} P(z_2) \\ U(z_2) \end{bmatrix} = \begin{bmatrix} \cos k_z(z_2 - z_1) & (i/Y)\sin k_z(z_2 - z_1) \\ iY \sin k_z(z_2 - z_1) & \cos k_z(z_2 - z_1) \end{bmatrix} \begin{bmatrix} P(z_1) \\ U(z_1) \end{bmatrix}. \tag{B12}$$

The values of k_z and Y are functions of the material parameters of the layer under consideration. In particular if c_n is the sound speed in layer n, ρ_n its density, k_r the horizontal wavenumber of the incident plane wave (by Snell's law common to all layers), and ω the temporal frequency of the cw source, then $k_n \equiv \omega/c_n$, $k_z = \sqrt{k_n^2 - k_r^2}$, and $Y = k_z/\omega\rho$.

$$\begin{bmatrix} P(z_2) \\ U(z_2) \end{bmatrix} = \Phi_n(z_2 - z_1) \begin{bmatrix} P(z_1) \\ U(z_1) \end{bmatrix}, \tag{B13}$$

when z_2 and z_1 are both within layer n.

To calculate the field at the top interface in terms of the field at the bottom interface, as shown in Fig. B1, we can use the previous discussion which was applicable only to a single layer, to relate the field at z_n to the field at z_{n-1}:

$$\begin{bmatrix} P(z_{n-1}) \\ U(z_{n-1}) \end{bmatrix} = \Phi_n(z_{n-1} - z_n) \begin{bmatrix} P(z_n) \\ U(z_n) \end{bmatrix} \equiv \Phi_n \begin{bmatrix} P(z_n) \\ U(z_n) \end{bmatrix}. \tag{B14}$$

We then iterate the procedure through all the layers to find

$$\begin{bmatrix} P(z_0) \\ U(z_0) \end{bmatrix} = \Phi_1 \Phi_2 \cdots \Phi_n \begin{bmatrix} P(z_n) \\ U(z_n) \end{bmatrix} \equiv \Phi \begin{bmatrix} P(z_n) \\ U(z_n) \end{bmatrix}. \tag{B15}$$

B. Numerical implementation

1. The modified propagation matrix

The bulk of computation associated with the propagator matrix approach is the accumulation of the matrices $\Phi_1 \Phi_2 \cdots \Phi_n$. When these are accumulated on the computer, the actual operation is $\Phi_1[\Phi_2(\cdots \Phi_N)]$. It is possible for the scale of the accumulated product to differ dramatically from any given Φ_i, particularly in the evanescent wave region, where the solutions in each layer are growing and decaying exponentials. Because of the limited dynamic range in the computer it is advisable to scale terms to make them comparable before accumulation. Fortunately the final calculation for the reflection coefficient depends only on ratios of elements in Φ. For this reason we normalize each of the Φ_i so that its largest value equals 1. This procedure alone could cause another problem stemming from the different scales in general for P and U, which is due to their different units. To bring P and U into the same units we do not actually relate

$$\begin{bmatrix} P(z_{n-1}) \\ U(z_{n-1}) \end{bmatrix} \text{ to } \begin{bmatrix} P(z_n) \\ U(z_n) \end{bmatrix}, \tag{B16}$$

but rather consolidate units by multiplying the normal component of velocity by the characteristic impedance for oblique incidence of that layer. Therefore we actually calculate

$$\begin{bmatrix} P(z_0) \\ \zeta_0 U(z_0) \end{bmatrix} = \begin{bmatrix} a_1 & b_1 \\ \xi_1 b_1 & \xi_1 a_1 \end{bmatrix} \cdots \begin{bmatrix} a_N & b_N \\ \xi_N b_N & \xi_N a_N \end{bmatrix} \begin{bmatrix} P(z_N) \\ \zeta_N U(z_N) \end{bmatrix}, \tag{B17}$$

where

$$k_{z,i} \equiv \sqrt{(\omega/c_i)^2 - k_r^2},$$
$$\zeta_i \equiv \omega \rho_i / k_{z,i} \equiv 1/Y_i,$$
$$\xi_i \equiv (\zeta_{i-1})/\zeta_i,$$
$$a_i \equiv \cos k_{z,i}(z_i - z_{i-1}),$$
$$b_i \equiv -i \sin k_{z,i}(z_i - z_{i-1}).$$

2. Relation of the modified propagation matrix to the incident and reflected waves

We now relate the field variables to the incident plane wave and the resulting reflected plane wave by slightly modifying Eq. (B10). We assume that the top interface is at $z = 0$ so that

$$\begin{bmatrix} P(0) \\ \zeta_0 U(0) \end{bmatrix} = \begin{bmatrix} 1 & 0 \\ 0 & \zeta_0 \end{bmatrix} \begin{bmatrix} 1 & 1 \\ Y_0 & -Y_0 \end{bmatrix} \begin{bmatrix} P_{+,0} \\ P_{-,0} \end{bmatrix} \tag{B18}$$

and

$$\begin{bmatrix} P_{+,0} \\ P_{-,0} \end{bmatrix} = \frac{1}{2} \begin{bmatrix} 1 & 1/Y_0 \\ 1 & -1/Y_0 \end{bmatrix} \begin{bmatrix} 1 & 0 \\ 0 & Y_0 \end{bmatrix} \begin{bmatrix} P(0) \\ \zeta_0 U(0) \end{bmatrix}. \tag{B19}$$

By defining

$$\begin{bmatrix} \phi_{11} & \phi_{12} \\ \phi_{21} & \phi_{22} \end{bmatrix} \equiv \prod_{i=1}^{N} \begin{bmatrix} a_i & b_i \\ \xi_i b_i & \xi_i a_i \end{bmatrix} \tag{B20}$$

and using Eq. (B17) we have

$$\begin{bmatrix} P_{+,0} \\ P_{-,0} \end{bmatrix} = \frac{1}{2} \begin{bmatrix} 1 & 1 \\ 1 & -1 \end{bmatrix} \begin{bmatrix} \phi_{11} & \phi_{12} \\ \phi_{21} & \phi_{22} \end{bmatrix} \begin{bmatrix} P(z_N) \\ \zeta_N U(z_N) \end{bmatrix}. \tag{B21}$$

We now need to use the fact that the pressure and velocity fields in the last layer are made up of only positive traveling waves so that [referring to Eq. (B10)] $P_{N+1} = P(z_N)$ and $U_{N+1} = (1/\zeta_{N+1})P(z_N)$ and we have

$$\begin{bmatrix} P_{+,0} \\ P_{-,0} \end{bmatrix} = \frac{1}{2} \begin{bmatrix} \phi_{11} + \phi_{21} & \phi_{12} + \phi_{22} \\ \phi_{11} - \phi_{21} & \phi_{12} - \phi_{22} \end{bmatrix} \begin{bmatrix} 1 \\ \zeta_N/\zeta_{N+1} \end{bmatrix} P_{N+1}. \tag{B22}$$

If we now use

$$\xi_{N+1} \equiv \zeta_n/\zeta_{N+1} \tag{B23}$$

we have the reflection coefficient

$$\Gamma = \frac{P_{-,0}}{P_{+,0}} = \frac{\phi_{11} - \phi_{21} + \xi_{N+1}(\phi_{12} - \phi_{22})}{\phi_{11} + \phi_{21} + \xi_{N+1}(\phi_{12} + \phi_{22})}. \tag{B24}$$

Equations (B19) and (B24) show that this approach uses only the ratios of the impedances in adjacent layers and never the impedances themselves. These ratios are much better behaved in general than the individual impedances. For this reason, because of the use of P and ζU instead of P and U, and because of the scaling of the layer propagation matrices this implementation of the propagator matrix approach has good numerical properties.

APPENDIX C: THE VALUE OF THE KERNEL FOR THE NUMERICAL PORTION OF THE HYBRID ALGORITHM AT THE WATER WAVENUMBER

In this appendix we derive the value of $L(k_0)$ discussed in Sec. III. $L(k_r)$ is defined in that section by Eq. (29) as

$$L(k_r) \equiv \{i[\Gamma(k_r) - \Gamma(k_0)]/\sqrt{k_0^2 - k_r^2}\} \times \exp(i\sqrt{k_0^2 - k_r^2}\,|z|), \tag{C1}$$

where we use $|z|$ here in place of $|z + z_0|$ in the text. We seek to evaluate the limit

$$\lim_{k_r \to k_0} L(k_r) \tag{C2}$$

under the condition that the impedance of the bottom, $Z(k_r)$, is finite at $k_r = k_0$.

At $k_r = k_0$ Eq. (C1) takes the indeterminate form 0/0. We evaluate the limit in Eq. (C2) by using L'Hopital's rule:

$$\lim_{k_r \to k_0} \{i[\Gamma(k_r) - \Gamma(k_0)] \exp(i\sqrt{k_0^2 - k_r^2}|z|)/\sqrt{k_0^2 - k_r^2}\}$$
$$= \lim_{k_r \to k_0} \left(\frac{\partial}{\partial k_r} i[\Gamma(k_r) - \Gamma(k_0)] \exp(i\sqrt{k_0^2 - k_r^2}|z|)\right)$$
$$\times \left(\frac{\partial}{\partial k_r}\sqrt{k_0^2 - k_r^2}\right)^{-1}. \quad \text{(C3)}$$

After separating out the terms that approach zero as $k_r \to k_0$ this expression becomes

$$\lim_{k_r \to k_0} L(k_r) = \lim_{k_r \to k_0} (-i\sqrt{k_0^2 - k_r^2}/k_r)\dot{\Gamma}(k_r)$$
$$\times \exp(i\sqrt{k_0^2 - k_r^2}|z|), \quad \text{(C4)}$$

where $\dot{\Gamma}(k_r) = \partial\Gamma(k_r)/\partial k_r$.

We now express $\dot{\Gamma}(k_r)$ in terms of the characteristic impedance at oblique incidence of the upper half-space, ζ_0, and the impedance at the interface which we will denote as Z_1. Both ζ_0 and Z_1 are functions of k_r in general. In terms of these $\Gamma(k_r)$ is given by

$$\Gamma(k_r) = (Z_1 - \zeta_0)/(Z_1 + \zeta_0). \quad \text{(C5)}$$

Taking derivatives we find

$$\dot{\Gamma}(k_r) = 2[(\dot{Z}_1\zeta_0 - Z_1\dot{\zeta}_0)/(Z_1 + \zeta_0)^2]. \quad \text{(C6)}$$

We now use the characteristic impedance of the upper half-space

$$\zeta_0 = \rho_0\omega/\sqrt{k_0^2 - k_r^2}, \quad \text{(C7)}$$

where ρ_0 is the density of the half-space, ω is the temporal frequency, and $k_0 \equiv \omega/C_0$ where C_0 is the speed of sound in the upper half-space. Substituting Eq. (C7) into Eq. (C6) and evaluating $\dot{Z}_0$ we have

$$\dot{\Gamma}(k_r) = 2\left(\frac{\dot{Z}_1(\rho_0\omega/\sqrt{k_0^2 - k_r^2}) - [k_r\rho_0\omega/(k_0^2 - k_r^2)^{3/2}]Z_1}{Z_1^2 + 2Z_1(\rho_0\omega/\sqrt{k_0^2 - k_r^2}) + \rho_0^2\omega^2/(k_0^2 - k_r^2)}\right) = 2\left(\frac{\sqrt{k_0^2 - k_r^2}\dot{Z}_1\rho_0\omega - (k_r\rho_0\omega/\sqrt{k_0^2 - k_r^2})Z_1}{Z_1^2(k_0^2 - k_r^2) + 2Z_1\rho_0\omega\sqrt{k_0^2 - k_r^2} + \rho_0^2\omega^2}\right). \quad \text{(C8)}$$

Substituting (C8) into (C4) we find

$$\lim_{k_r \to k_0} L(k_r) = \lim_{k_r \to k_0}\left(\frac{-i\sqrt{k_0^2 - k_r^2}}{k_r} 2\frac{\sqrt{k_0^2 - k_r^2}\rho_0\omega\dot{Z}_1 - (k_r\rho_0\omega/\sqrt{k_0^2 - k_r^2})Z_1}{Z_1^2(k_0^2 - k_r^2) + 2Z_1\rho_0\omega(k_0^2 - k_r^2)^{1/2} + \rho_0^2\omega^2}\right) \quad \text{(C9)}$$

or

$$L(k_0) = -2iZ_1(k_0)/\rho_0\omega \quad \text{(C10)}$$

provided that $\lim_{k_r \to k_0}(k_0^2 - k_r^2)\dot{Z}_1(k_r) = 0$.

If the interface is between two isovelocity half-spaces, the expression (C10) for $L(k_0)$ can be written directly in terms of the material parameters. For this case $Z_1(k_r) = \rho_1\omega/\sqrt{k_1^2 - k_r^2}$. $Z_1(k_0)$ is finite because $k_1 \neq k_0$ (if $k_1 = k_0$ there would be no interface). At the interface between two isovelocity half-spaces, $L(k_0)$ is therefore given by

$$L(k_0) = -2i\rho_1/\rho_0\sqrt{k_1^2 - k_0^2}. \quad \text{(C11)}$$

APPENDIX D: EVALUATION OF THE POLE CONTRIBUTION TO THE FIELD FOR SEC. III B

Here we evaluate the pole contribution to Eq. (31):

$$I(r, z; \rho_i) \equiv \int_0^\infty \frac{1}{\rho^2 - \rho_i^2}\frac{i}{(k^2 - \rho^2)^{1/2}}\exp(i\sqrt{k^2 - \rho^2}|z|)\, J_0(\rho r)\rho\, d\rho, \quad \text{(D1)}$$

where we use $|z|$ in place of $|z + z_0|$, which was used in the body of this paper. We evaluate Eq. (D1) by determining a partial differential equation that it satisfies and solving that equation.

Taking the second partial derivative of Eq. (D1) with respect to z we have

$$\frac{\partial^2}{\partial z^2} I(r, z; \rho_i) = \int_0^\infty \frac{\rho^2 - k^2}{\rho^2 - \rho_i^2}\frac{i}{(k^2 - \rho^2)^{1/2}}\exp(i\sqrt{k^2 - \rho^2}|z|)\, J_0(\rho r)\rho\, d\rho + 2\delta(z)$$
$$\times \int_0^\infty \frac{i\sqrt{k^2 - \rho^2}}{\rho^2 - \rho_i^2}\frac{i}{(k^2 - \rho^2)^{1/2}}\exp(i\sqrt{k^2 - \rho^2}|z|)\, J_0(\rho r)\rho\, d\rho. \quad \text{(D2)}$$

If we use

$$\delta(z)f(z) = \delta(z)f(0) \quad \text{for any } f(z), \quad \text{(D3)}$$

then Eq. (D2) becomes

$$\frac{\partial^2}{\partial z^2} I(r, z; \rho_i) = \int_0^\infty \frac{\rho^2 - k^2}{\rho^2 - \rho_i^2}\frac{i}{(k^2 - \rho^2)^{1/2}}\exp(i\sqrt{k^2 - \rho^2}|z|)\, J_0(\rho r)\rho\, d\rho - 2\delta(z)\int_0^\infty \frac{1}{\rho^2 - \rho_i^2} J_0(\rho r)\rho\, d\rho. \quad \text{(D4)}$$

Putting it all together we have

$$\left(\frac{\partial^2}{\partial z^2}-(\rho_i^2-k^2)\right)I(r,z;\rho_i)=\int_0^\infty \frac{i}{(k^2-\rho_i^2)^{1/2}}\exp(i\sqrt{k^2-\rho^2}\,|z|)\,J_0(\rho r)\rho\,d\rho-2\delta(z)\int_0^\infty \frac{1}{\rho^2-\rho_i^1}J_0(\rho r)\rho\,d\rho. \tag{D5}$$

If we define $\beta^2\equiv\rho_i^2-k^2$, choosing real part of $\beta>0$, and using

$$\int_0^\infty \frac{i}{(k^2-\rho^2)^{1/2}}\exp(i\sqrt{k^2-\rho^2}\,|z|)\,J_0(\rho r)\rho\,d\rho=\exp(ik\sqrt{r^2+z^2})/\sqrt{r^2+z^2} \tag{D6}$$

together with

$$\int_0^\infty \frac{1}{\rho^2-\rho_i^2}J_0(\rho r)\rho\,d\rho=K_0\{-\operatorname{sgn}[\operatorname{Im}(\rho_i)]i\rho_i r\}=\frac{-\pi i}{2}H_0^{(1)}(\rho_i r),\quad \text{when } \operatorname{Im}(\rho_i)>0, \tag{D7}$$

where

$$\operatorname{sgn}(x)=\begin{cases}-1, & x<0,\\ 1, & z>0,\end{cases}$$

Eq. (D5) becomes

$$\left(\frac{\partial^2}{\partial z^2}-\beta^2\right)I(r,z;\rho_i)=\frac{\exp(ik\sqrt{r^2+z^2})}{r^2+z^2}+i\pi\delta(z)H_0^{(1)}(\rho_i r), \tag{D8}$$

when $\operatorname{Im}(\rho_i)>0$.

The Green's function for this differential equation is given by

$$G(r,z,\xi)=(-1/2\beta)e^{-|z-\xi|\beta}. \tag{D9}$$

Using this for the impulsive response and convolving with the continuous driving function to obtain the particular solution we obtain

$$I(r,z;\rho_i)=\frac{-1}{2\beta}\int_{-\infty}^{\infty}\frac{\exp(ik\sqrt{r^2+\xi^2})}{(r^2+\xi^2)^{1/2}}e^{-\beta|z-\xi|}\,d\xi-\frac{i\pi}{2\beta}H_0^{(1)}(\rho_i r)e^{-\beta|z|}, \tag{D10}$$

when $\operatorname{Im}(\rho_i)>0$.

The general form of this expression which is valid for all ρ_i is given by

$$I(r,z;\rho_i)=\frac{-1}{2\beta}\int_{-\infty}^{\infty}\frac{\exp(ik\sqrt{r^2+\xi^2})}{(r^2+\xi^2)^{1/2}}e^{-\beta|z-\xi|}\,d\xi+\frac{1}{\beta}K_0\{-\operatorname{sgn}[\operatorname{Im}(\rho_i)]i\rho_i r\}e^{-\beta|z|}, \tag{D11}$$

where $K_0(\cdot)$ is the modified Bessel function of order O.

[1] L. Brekhovskikh, *Waves in Layered Media* (Academic, New York, 1960).
[2] K. Aki and P. G. Richards, *Quantitative Seismology Theory and Methods* (Freeman, San Francisco, 1980).
[3] J. R. Wait, *Electromagnetic Waves in Stratified Media* (Pergamon, New York, 1970).
[4] L. B. Felsen and N. Marcuvitz, *Radiation and Scattering of Waves* (Prentice-Hall, Englewood Cliffs, NJ, 1973).
[5] I. Tolstoy and C. S. Clay, *Ocean Acoustics: Theory and Experiment in Underwater Sound* (McGraw-Hill, New York, 1966).
[6] A. V. Oppenheim and R. Schafer, *Digital Signal Processing* (Prentice-Hall, Englewood Cliffs, NJ, 1975).
[7] D. R. Mook, "The Numerical Synthesis and Inversion of Acoustic Fields Using the Hankel Transform with Application to the Estimation of the Plane Wave Reflection Coefficient of the Ocean Bottom," ScD thesis MIT/WHOI Joint Program, Cambridge, MA, and Woods Hole, MA (January 1983).
[8] G. V. Frisk, A. V. Oppenheim, and D. Martinez, "A Technique for Measuring the Plane-Wave Reflection Coefficient of the Ocean Bottom," J. Acoust. Soc. Am. **68**, 602–612 (1980).
[9] G. V. Frisk, D. R. Mook, J. A. Doutt, E. E. Hays, and A. V. Oppenheim, "The Application to Real Data of a Technique for Measuring the Plane-Wave Reflection Coefficient of the Ocean Bottom," J. Acoust. Soc. Am. Suppl. 1 **72**, S97 (1982).
[10] D. C. Stickler, "Inverse Scattering in a Stratified Medium," J. Acoust. Soc. Am. **74**, 994–1005 (1983).
[11] G. V. Frisk, J. Doutt, and E. Hays, "Bottom Interaction of Low-Frequency Acoustic Signals at Small Grazing Angles in the Deep Ocean," J. Acoust. Soc. Am. **69**, 84–94 (1981).
[12] F. R. DiNapoli, "A Fast Field Program for Multilayered Media," NUSC Tech. Rep. 4103, New London, CT (1971).
[13] F. R. DiNapoli and R. L. Deavenport, "Theoretical and Numerical Green's Function Field Solution in a Plane Multilayered System," J. Acoust. Soc. Am. **67**, 92–105 (1980).
[14] L. Tsang, R. Brown, J. A. Kong, and G. Simmons, "Numerical Evaluation of Electromagnetic Fields Due to Dipole Antennas in the Presence of Stratified Media," J. Geophys. Res. **79**, 2077–2080 (1974).
[15] A. E. Siegman, "Quasi-Fast Hankel Transform," Opt. Lett. **1**, 13–15 (1977).
[16] A. V. Oppenheim, G. V. Frisk, and D. R. Martinez, "An Algorithm for the Numerical Evaluation of the Hankel Transform," Proc. IEEE **66**, 264–265 (1978).
[17] W. L. Anderson, "Computer Program Numerical Integration of Related Hankel Transforms of Orders 0 and 1 by Adaptive Digital Filtering," Geophysics **44**, 1287–1305 (1979).
[18] E. Cavanagh and B. D. Cook, "Numerical Evaluation of Hankel Transforms via Gaussian-Laguerre Polynomial Expansions," IEEE ASSP **27**, 361–366 (1979).
[19] H. K. Johansen and K. Sorensen, "Fast Hankel Transforms," Geophys. Prosp. **27**, 876–901 (1979).
[20] A. V. Oppenheim, G. V. Frisk, and D. Martinez, "Computation of the

Hankel Transform Using Projections," J. Acoust. Soc. Am. **68**, 523–529 (1980).
[21]D. R. Mook, "An Efficient Algorithm for the Numerical Evaluation of the Hankel and Abel Transforms," IEEE Trans. Acoust., Speech, Signal Process. **ASSP-31**, 979–985 (1983).
[22]J. Brunol and P. Chavel, "Fourier Transformation of Rotationally Invariant Two-Variable Functions: Computer Implementation of Hankel Transform," Proc. Letters IEEE **65**, 1089–1090 (1977).
[23]S. M. Candel, "Dual Algorithms for Fast Calculation of the Fourier–Bessel Transform," IEEE ASSP **29**(5), 963–972 (1981).
[24]G. N. Watson, *Theory of Bessel Functions* (Cambridge U.P., New York, 1966), 2nd. ed.
[25]W. H. Young, "On Series of Bessel Functions," Proc. London Math. Soc. **2 XVIII**, 163–200 (1920).
[26]L. Lipschitz, J. Math. **56**, 189–196 (1859).
[27]F. R. DiNapoli, "Acoustic Propagation in a Stratified Medium," NUSC Tech. Rep. 1046, New London, CT (1969).
[28]D. S. Ahluwalia and J. B. Keller, "Exact and Asymptotic Representations of the Sound Field in a Stratified Ocean," in *Wave Propagation and Underwater Acoustics*, edited by J. B. Keller and J. S. Papadakis (Springer, Berlin, 1977), Lecture Notes in Physics, Vol. 70.
[29]H. P. Bucker, "Sound Propagation in a Channel with Lossy Boundaries," J. Acoust. Soc. Am. **48**, 1187–1194 (1970).
[30]H. P. Bucker, "Propagation in a Liquid Layer Lying Over a Liquid Half-Space (Pekeris Cut)," J. Acoust. Soc. Am. **65**, 906–908 (1979).
[31]D. C. Stickler, "Normal-Mode Program with both the Discrete and Branch Line Contributions," J. Acoust. Soc. Am. **57**, 856–861 (1975).
[32]D. C. Stickler and E. Ammicht, "Uniform Asymptotic Evaluation of the Continuous Spectrum Contribution for the Pekeris Model," J. Acoust. Soc. Am. **67**, 2018–2024 (1980).
[33]M. Macpherson and G. V. Frisk, "The Contribution of Normal Modes in the Bottom to the Acoustic Field in the Ocean," J. Acoust. Soc. Am. **68**, 929–940 (1980).
[34]This is the case when the vertical dimensions of the layers become large compared to a wavelength.
[35]H. Weinberg, "Application of Ray Theory to Acoustic Propagation in Horizontally Stratified Oceans," J. Acoust. Soc. Am. **58**, 97–109 (1975).
[36]T. Tamir and L. B. Felsen, "On Lateral Waves in Slab Configurations and their Relation to other Wave Types," IEEE Trans. Antennas Propag. **AP-13**, 410–422 (1965).
[37]C. T. Tindle and K. M. Guthrie, "Rays as Interfering Modes in Underwater Acoustics," J. Sound Vib. **34**, 291–295 (1974).
[38]K. Fuchs and G. Müller, "Computation of Synthetic Seismograms with the Reflectivity Method and Comparison with Observations," Geophys. J. R. Astron. Soc. **23**, 417–433 (1971).
[39]R. Stephen, "Synthetic Seismograms For the Case of the Receiver Within the Reflectivity Zone," Geophys. J. R. Astron. Soc. **51**, 169–181 (1977).
[40]R. Bracewell, *The Fourier Transform and Its Applications* (McGraw-Hill, New York, 1965).
[41]A. Papoulis, *Systems and Transforms with Applications in Optics* (McGraw-Hill, New York, 1968).
[42]In the sense that its Hankel transform is zero outside some finite interval. This condition implies that its Fourier transform is also zero outside the same finite interval. This assumption is consistent with the physical constraints of measuring devices that provide data.
[43]These pictures were generated by applying Eq. (13), and not by actually performing the numerical transform. This was done to avoid the errors introduced primarily for small values of k_r by the use of the asymptotic method and to avoid the windowing affects associated with transforming.
[44]The minus sign is an effect of aliasing for the Fourier–Bessel series as seen in Appendix A.
[45]W. T. Thomson, "Transmission of Elastic Waves Through a Stratified Solid Medium," J. Appl. Phys. **21**, 89–93 (1950).
[46]N. A. Haskell, "The Dispersion of Surface Waves in Multilayered Media," Bull. Seismol. Soc. Am. **43**, 17–34 (1953).
[47]We show in Appendix C that if the impedance and its first derivative at the interface is finite for $k_r = k_0$ then the $\lim_{k_r \to k_0} L(k_r) = Z_1/\omega\rho_0$, where Z_1 is the impedance of the bottom at $k_r = k_0$, ω is $2\pi \cdot$ source frequency, and ρ_0 is the density of the water. For an isovelocity half-space this expression reduces to $L(k_0) = \rho_1/\rho_0\sqrt{k_1^2 - k_0^2}$, which is finite.
[48]Such a pole can only appear in the interval $k_0 < k_r < k_1$.
[49]G. V. Frisk, "Inhomogeneous Waves and the Plane-Wave Reflection Coefficient," J. Acoust. Soc. Am. **66**, 219–234 (1979).
[50]We will call two functions equal if the Fourier transform of their difference has no energy at any finite frequency. For this reason we need not single out the values of $P(r)$ in Eq. (A1) at points of discontinuity.
[51]This differs from Watson's presentation of Schlafli's result.
[52]Schlafli does not restrict the region of validity of his result. Watson, however, states that Schlafli's result proceeds from a formula which is strictly valid only for $0 < r + \xi < 2$ and $r \neq \xi$. We will later plot $T_{128}(r,\xi)$ to show that the results of this analysis appear valid inside the region $0 < r + \xi \leqslant 2$ and approximately valid outside that region.
[53]L. Schlafli, "Ueber die Convergenz der Entwicklung einer Arbitraren Function $f(x)$ nach den Bessel'schen Functionen $J_a(\beta_1 x),...,$" Math. Ann. **X**, 137–142 (1876).
[54]This can be seen by examining the limit of the sequence of Fourier transforms. Each transform is zero in the interval $(-N/2, N/2)$. For any band-limited function N_0 can always be made big enough that the result of convolving it with $[\cos N\pi x/\sin(\pi x/2)]\sin \pi x/4$ is zero for $N > N_0$. As a generalized function the limit in Eq. (A10) is therefore zero.
[55]We have included the point $r + \xi = 2$, which is not strictly within the interval specified by Watson.
[56]L. L. Beranek, *Acoustics* (McGraw-Hill, New York, 1954).